

PARTICLE DETECTION METHODS*

BY K. KLEINKNECHT

Institut für Physik der Universität Dortmund, Dortmund**

(Received October 3, 1980)

The principles of detectors are discussed following the list of the basic quantities to be measured by experiment: position, time and identity, energy and momentum.

PACS numbers: 29.40.-n

I. INTRODUCTION

Progress in experimental particle physics has always been closely correlated with improvements in accelerator and detector technology. In the last ten years, we have seen several breakthroughs in these fields. In accelerator technique there was the construction of storage rings and the invention of stochastic and electron-cooling, in the field of detectors the proportional chamber in its various forms has made possible electronic detectors with good space and time resolution, and the capacity for control and processing of data has been increasing drastically by fast on-line and off-line computers.

In these lectures, I will go through the basic principles of detectors without too much emphasis on details. The structure of the lectures follows the list of basic quantities to be measured by experiment: position, time and identity, energy and momentum.

The article is subdivided as follows:

II. Position

II.1. Physical processes for detection

II.2. Proportional chambers

II.3. Drift chambers

II.4. Time projection chamber

II.5. Bubble, streamer and flash chambers

II.6. Comparison of position chambers

III. Time and identity

III.1. Photomultiplier

III.2. Scintillators

III.3. Light collection

* Presented at the XX Cracow School of Theoretical Physics, Zakopane, May 29—June 11, 1980.

** Address: Institut für Physik der Universität Dortmund, 4600 Dortmund 50, Federal Republic Germany.

III.4. Time-of-flight

III.5. Čerenkov counters

III.6. Transition radiation detectors

III.7. Multiple ionization measurement

III.8. Comparison of identification methods

IV. Energy

IV.1. Electron photon shower counters

IV.2. Hadron calorimeters

IV.3. Monitoring of calorimeters

V. Momentum

V.1. Magnet shapes for fixed target experiments

V.2. Magnet shapes for storage ring experiments

VI. Realization of detector systems

VI.1. A hadron beam detector

VI.2. A neutrino detector

VI.3. A storage ring detector

In writing up these lectures I profited from the recent review by Fabjan and Fischer [1].

II. POSITION

II.1. Physical processes for detection

The physical processes which enable us to detect particles are different for neutral and charged particles. Photons can interact by photoelectric or Compton effect or by pair creation, where the latter process dominates at high energies. The resulting electrons and positrons can be detected by their electromagnetic interaction. Neutrons of high energy will produce a shower of hadrons when colliding with detector material, thus enabling the detection of charged secondaries. Neutrinos interact by weak interaction conserving lepton number, producing hadrons and a charged or neutral lepton.

In contrast to these neutral particles, charged particles can be detected without undergoing any other process than electromagnetic interaction with the atomic electrons of the detector material. In these collisions, the energy loss of the charged particle by ionization is given by the Bethe-Bloch-formula [2]:

$$-dE/dx = (4\pi N_0 Z z^2 e^4 / (m_e v^2 A) [\ln(2m_e v^2 / (I(1 - \beta^2))) - \beta^2],$$

where x is the thickness of material traversed in $\text{g} \cdot \text{cm}^{-2}$, N_0 is Avogadro's number, Z and A are atomic mass numbers of the material, ze and $v = \beta/c$ the charge and velocity of the moving particle, m_e the electron mass and I an effective atomic ionization potential. The dependence of this energy loss on particle velocity is characterized by the $1/v^2$ variation at low energies, by a minimum at $\beta\gamma = p/mc \approx 3$ and finally, at high energies, by the relativistic rise by a factor which, for gases, is around 1.5. Fig. 1 shows this behaviour as measured [3] in an Argon-Methane mixture. The data are reproduced well by the calculated curve.

The energy loss by ionization is distributed statistically around the mean loss described by the Bethe-Bloch-formula, the distribution being asymmetric with a tail [4] at high losses due to δ ray production and distant collisions.

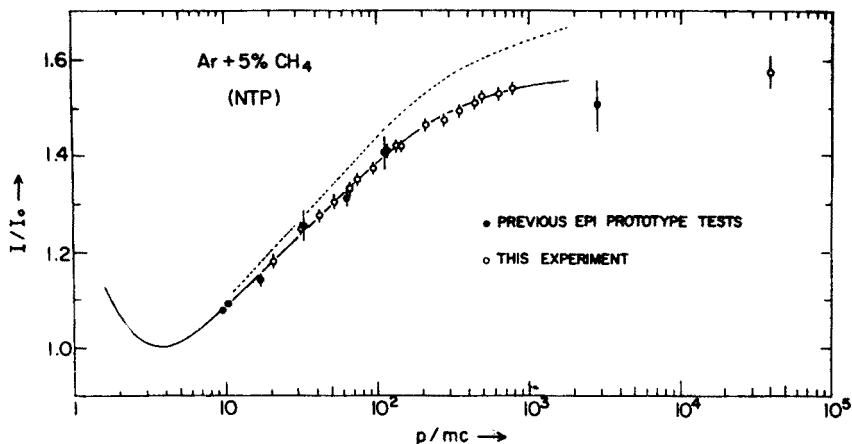


Fig. 1. Mean energy loss as a function of $\beta\gamma$ of the charged particle, measured by multiple ionization sampling (Ref. [3])

The average energy needed for creating an electron-ion pair is fairly similar in different gases, viz. 40 eV/pair in Helium and 26 eV in Argon, while it is much smaller in solids, e.g. 3 eV/pair for Si, such that for solids the number of pairs is larger and the statistical fluctuations in energy loss are smaller. However, the technical problems with the production of large volumes of purified semiconductors have limited the use of Si and Ge counters to low-energy high resolution γ spectroscopy. For detection of charged particles in large area chambers we are left with ionization in gases, mainly noble gases.

II.2. Proportional chambers

Proportional tubes had been used since a long time. A cylindrical tube (radius r_a) on negative potential and a central wire (radius r_i) on positive potential create an electric field of the form

$$E(r) = V_0 / (r \ln r_a / r_i),$$

which reaches $10^4 - 10^5$ V/cm near the anode wire. An electron liberated in an ionization process between two collisions at radial distances r_1 and r_2 gains the kinetic energy ΔT

$$\Delta T = e \int_{r_1}^{r_2} E(r) dr$$

and if ΔT exceeds the ionization energy of the gas atoms, a secondary ionization can take place. A chain of such processes leads to an avalanche of secondary electrons and ions. The number of secondary electrons per primary electron (gas amplification α) reaches $10^4 - 10^6$ in the proportional region, where α is independent of the number of primary electrons.

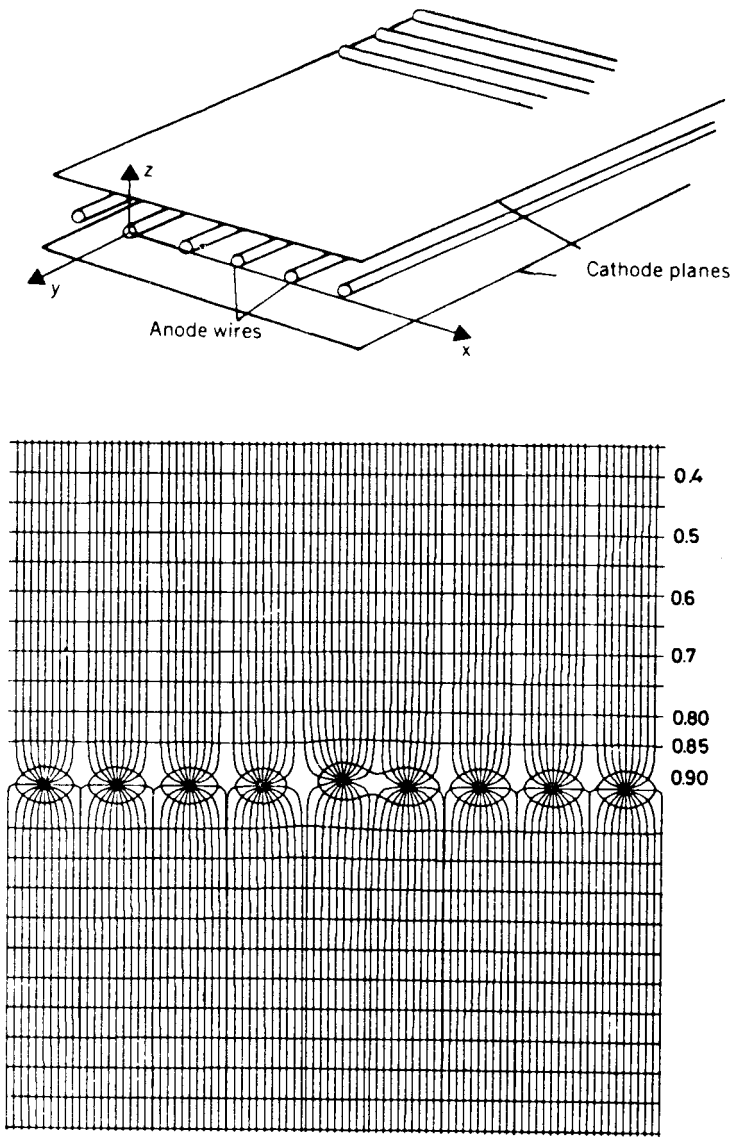


Fig. 2. Field configuration in a proportional chamber; field and equipotential lines are drawn (Ref. [5])

The field configuration in a proportional chamber with many anode wires in a plane between two cathode planes is shown in Fig. 2. The discovery of Charpak et al. [6] was that these separate anode wires act as independent detectors. The capacitive coupling of negative pulses from one wire to the next is negligible compared to the positive pulse on the neighbour wires induced by the moving avalanche. The main contribution does not come from the fast-moving electrons but from the much (1000 times) slower ions in the drop-shaped avalanche (Fig. 3). The time structure of the negative pulse induced on

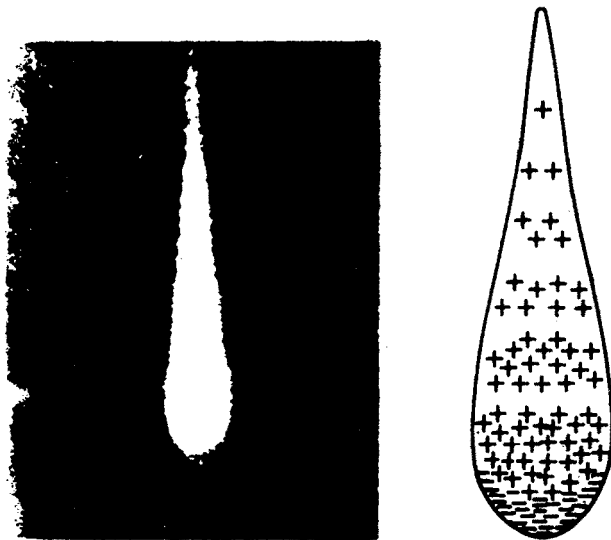


Fig. 3. Shape of the ionization avalanche in a high electric field (Ref. [7])

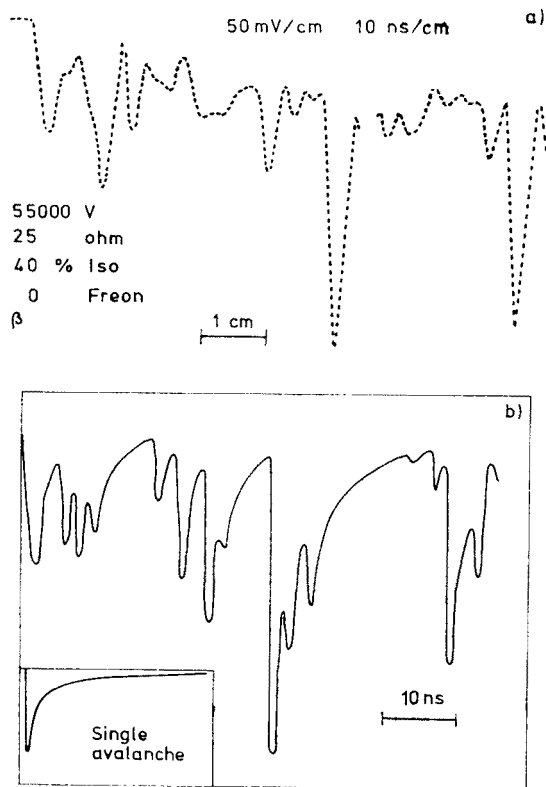


Fig. 4. a) Oscilloscope display of proportional chamber pulse showing separate avalanches. b) Pulse shape as simulated by computer (Ref. [8])

the anode wire creating the avalanches has been clarified subsequently [8]. It consists of several pulses induced by different avalanches created by different primary ionization electrons drifting one after another into the high field region near the anode wire. These pulses have typically a rise-time of 0.1 ns from the electron part and a decay time of 30 ns from the ion part of the avalanche. Fig. 4 shows an oscilloscope picture with a time resolution sufficient to resolve these separate pulses, which in normal applications are integrated into one pulse by slower amplifiers.

As a practical example for operating proportional chamber systems, one of the first spectrometers with large chambers [9] used a wire distance of 2mm, gold plated Tungsten wires of 20 μm , a gap between signal wires and cathode plane of 6mm and an Argon-Isobutane gas mixture. The amplifiers [10], based on MECL 1035 chips, had a threshold of 200 μV on 2 k Ω and an effective resolving time of 30 ns. The detection efficiency for this system, shown in Fig. 5, allows operating at full efficiency at 4.3 kV with a 40 ns sensitive time, i.e. the gate for the wire signals was opened by an external trigger for this time interval. The space resolution for this wire distance is $\sigma \sim 0.7$ mm.

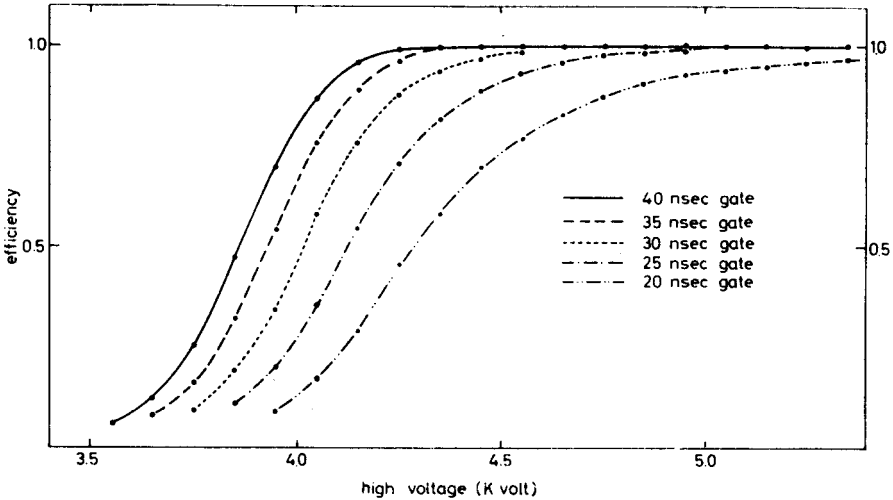


Fig. 5. Detection efficiency of a proportional chamber (2 mm wire distance, 2×6 mm gap) vs high voltage for different gate widths (Ref. [9])

One of the problems encountered in large chambers is the mechanical instability of the signal wires due to the electrostatic force between wires. It can be calculated [11] that the system is stable if the wire tension T exceeds a value given by the wire geometry

$$T > (Vl/2\pi a)^2/4\pi\epsilon_0,$$

where V is the potential difference between anode and cathode, l is the length of the signal wire, and a is the gap between wire and cathode plane. For the example above, with a wire tension of 50 p, the wires are stable for $l \leq 40$ cm. This means that for larger chambers

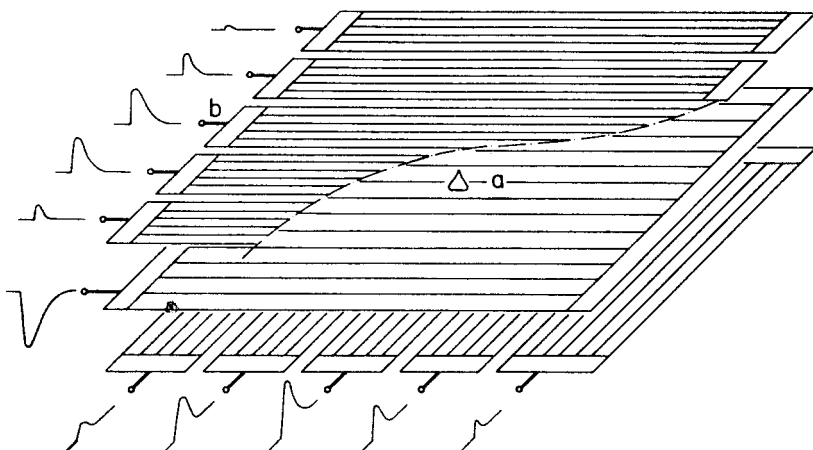


Fig. 6. Principle of cathode readout for proportional chambers. The center of gravity of the pulses on cathode strips determines the position of avalanche *a* (Ref. [14])

the wires have to be supported every 40 cm by support wires threaded across, or by other methods. An inefficiency of 10% in a region of 5 mm width around the support wire is a consequence of some of these schemes [12].

An enormous increase in spatial resolution of proportional chambers can be achieved by using the information from pulses induced on the cathode plane [13, 14]. For this purpose, at least one of the cathode planes is made of strips perpendicular to the direction of anode wires (see Fig. 6). The pulses induced by the avalanche on the individual strips vary with the distance of the strip from the avalanche, and the center of gravity of the inte-

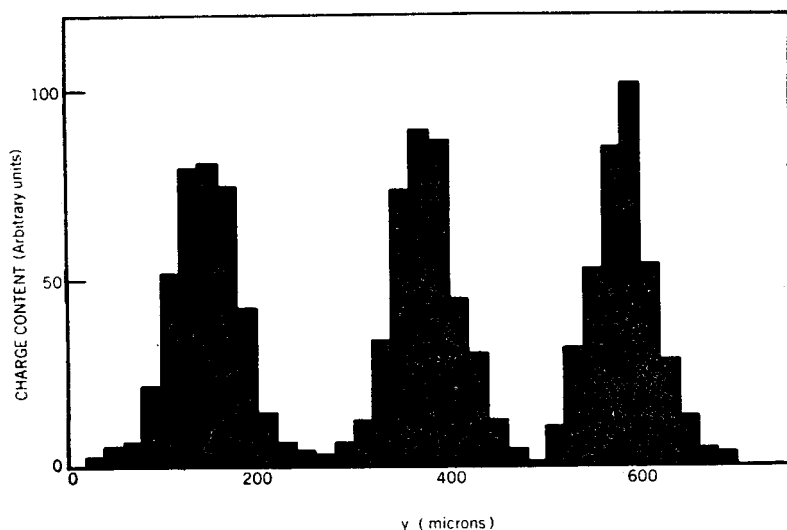


Fig. 7. Spatial resolution of a proportional chamber exposed to a 1.4 keV X-ray beam at 3 positions, 200 μ apart; plotted is total charge on cathode vs. center of gravity (Ref. [14])

grated pulse heights is a measure of the avalanche position. Fig. 7 demonstrates the precision which can be obtained with this center-of-gravity method. A soft X-ray produces ionization at three positions separated by 200 μm . The center of gravity y of each avalanche and the integrated charge c are measured, and the distribution in y shows three peaks with a variance of 35 μm . Most of this resolution error comes from the range of the original photoelectron. This impressive accuracy, however, is achieved with a detector where both mechanical construction and electronic pulse-height processing is costly.

II.3. Drift chambers

A great reduction in cost is possible by using the experimental fact [6] that the time delay between the crossing of a charged particle through a proportional chamber and the creation of a pulse on the anode wire is related to the distance between particle trajectory and anode wire. This delay was found to be of the order of 20 nsec/mm, and if this time is measured for each anode wire with an accuracy of 4 nsec, a spatial resolution of 200 μm can be obtained.

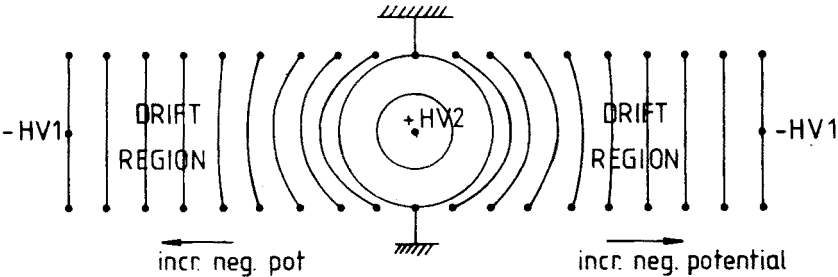


Fig. 8. Equipotential lines in a drift chamber cell

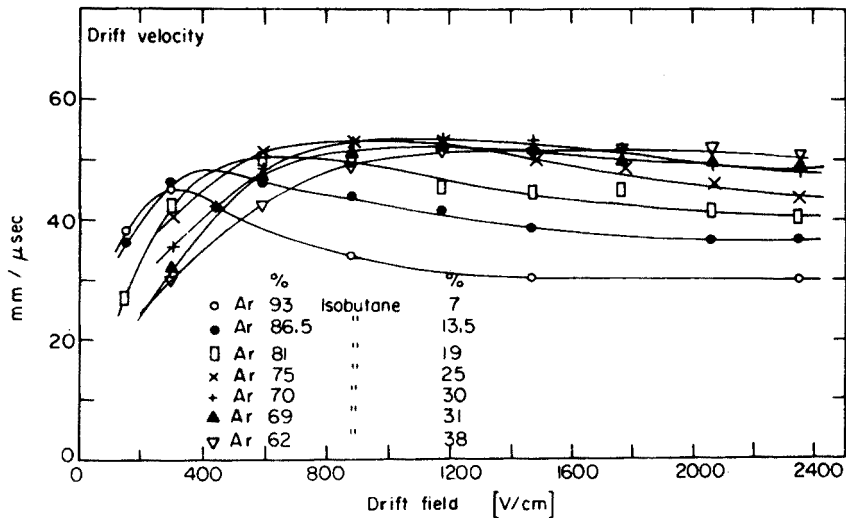


Fig. 9. Drift velocities in Argon-Isobutane mixtures (Ref. [17])

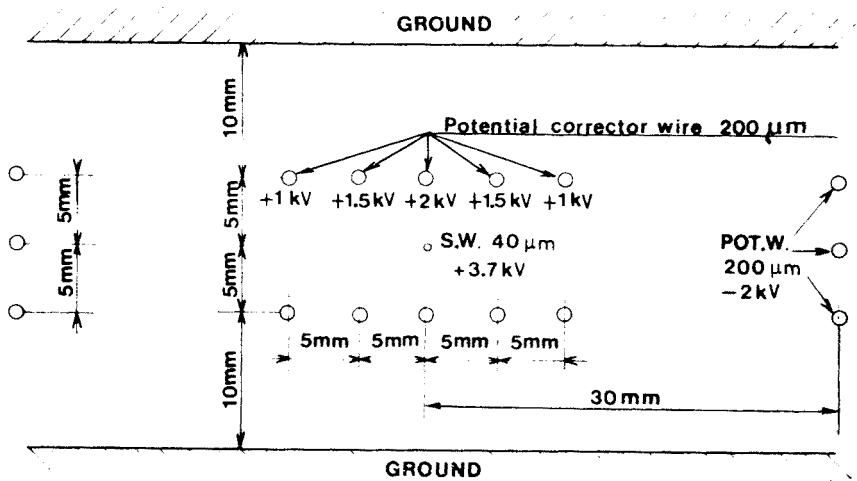


Fig. 10. Cell structure of large area drift chambers (Ref. [18])

The invention of the drift chamber [15, 16] exploits this possibility. A sketch of the field configuration in one cell of a drift chamber is shown in Fig. 8. The electrons from the primary ionization process drift in a low field (1000 V/cm) region into the high field amplification region around the anode wire, where avalanche formation occurs. Typical drift velocities for different gases are shown in Fig. 9 for various Argon-Isobutane mixtures [17]. For some of the mixtures, the drift velocity depends only mildly on the field strength, thus enabling a linear relation between distances and drift time even without constructing a perfectly constant field in the drift region. This is important because the requirement

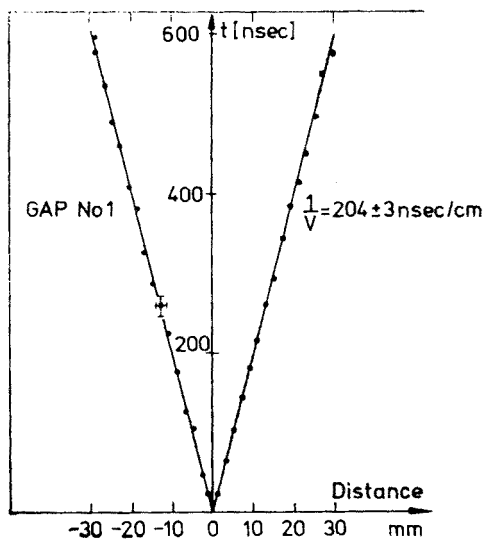


Fig. 11. Linear relation between drift time and position (Ref. [18])

of a constant drift field necessitates the introduction of several field shaping wires per cell. An example for such a cell [18] is shown in Fig. 10, where the cell dimensions are 60×30 mm. The linearity between drift time and distance for this chamber is shown in Fig. 11.

II.4. Time projection chamber

An ingenious way of using the proportional chamber principle for the central detector of a storage ring detector was proposed by Nygren [19]. Fig. 12 shows a large (1 m radius, 2 m length) cylindrical volume filled with Argon–Methane at 10 atmospheres. The two end caps are equipped with one layer of multiwire proportional chambers.

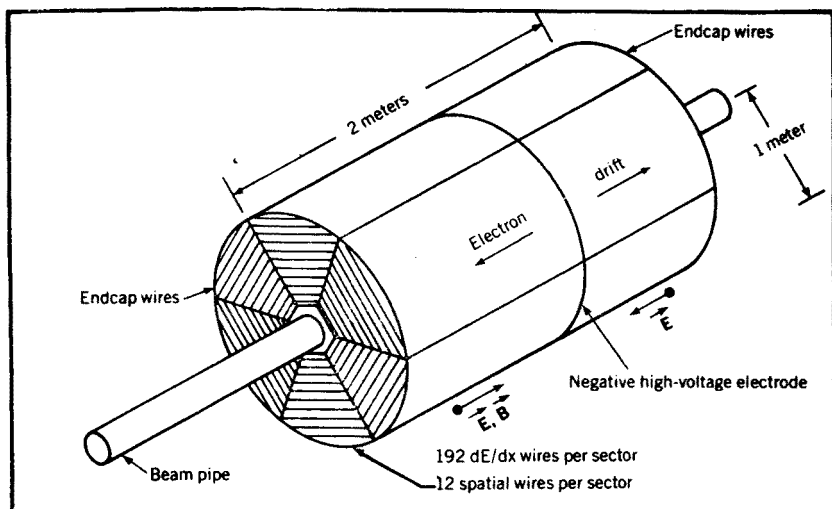


Fig. 12. Sketch of time projection chamber (Ref. [19])

Most importantly here, the electric drift field (150 kV/m) is parallel to the magnetic field (1.5 T) of the solenoid used for magnetic analysis of tracks originating from the collisions in the center of the cylinder. $\vec{E} \times \vec{B}$ type forces vanish, and it is possible to have the ionization electrons drift over these large distances to the end caps. Furthermore, the strong magnetic field reduces considerably (factor 10) the diffusion broadening of the track image on the end caps of the cylinder by causing helical movements of the electrons around the magnetic field lines.

The spatial reconstruction of the original tracks is obtained by measuring the two-dimensional images on the end-caps using the cathode plane readout and the center-of-gravity method and by measuring the drift time of each track segment parallel to the cylinder axis. In addition, the proportional chambers also measure the ionization energy loss of the track, thus enabling the separation of e , π , K and p by using dE/dx and momentum measurement.

II.5. Bubble, streamer and flash chambers

The bubble chamber is still unique in its capability of analyzing complicated events with many tracks and identifying those particles. A beautiful example for such a super-event is shown in Fig. 13. However, the use of bubble chambers as isolated detectors has diminished because (i) they cannot be employed at storage rings; (ii) at high energy showers are not contained in the chamber volume any more; (iii) the lever arm for momentum measurement is not sufficient at high momenta. Future use will include small chambers with extremely high resolution, e.g. the $6\text{ }\mu\text{m}$ resolution obtained by holographic readout in the BEBC chamber at CERN [21], used in conjunction with large spectrometers for momentum measurement and identification of reaction products ("Hybrid Systems").

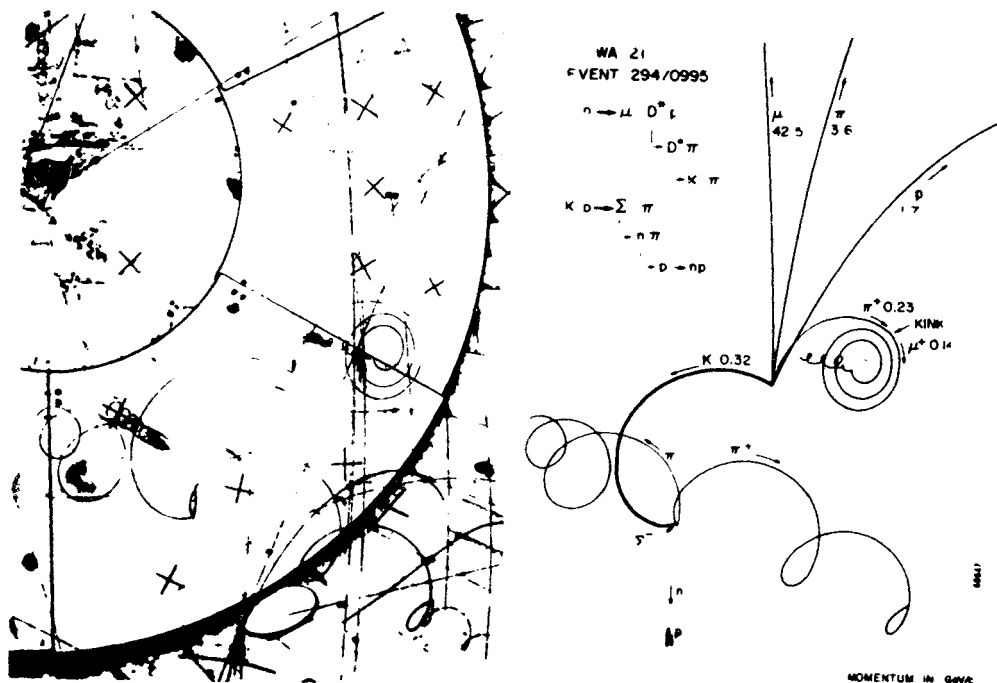


Fig. 13. Neutrino interaction in hydrogen bubble chamber BEBC (Ref. [20])

In a similar development streamer chambers are used as track sensitive targets. In this type of chamber very high electric fields perpendicular to the track direction create an avalanche with gas amplification around 10^8 and light emission ("streamer"). The geometry of such a chamber is given in Fig. 14. Very short high voltage pulses (few nsec) are required in order to keep the streamers short [21].

The excellent quality of streamer chambers presently in use can be seen in Fig. 15, a picture from the NA5 experiment at CERN [24]. The development of a very high resolution streamer chamber has been pioneered at Yale [25] in order to measure the lifetimes of charmed particles, around 10^{-13} sec, corresponding to a flight path of $300\text{ }\mu\text{m}$ for a time

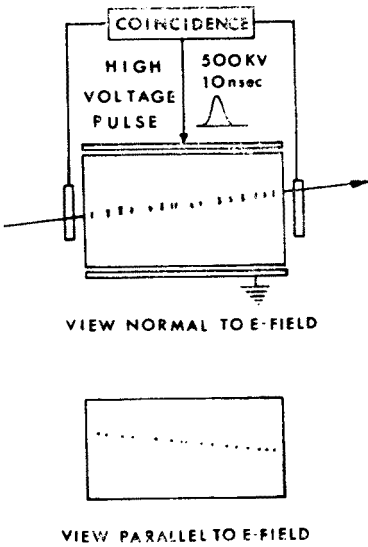


Fig. 14. Schematic view of streamer chamber (Ref. [22])

dilatation factor $\gamma = 10$ which is typical for a particle of 30 GeV/c with a mass of 3 GeV. This chamber operates at 24 atmospheres, uses pulses of 0.5 nsec duration producing a field of 330 kV/cm, and a spatial resolution of 32 μm has been achieved [26]. With this technique a good measurement of charmed particle lifetime seems feasible, competitive with similar experiments using nuclear emulsions.

Another gas discharge chamber is the flash chamber developed by Conversi et al. [27] and built in a similar way for the FMNN Neutrino experiment at Fermilab [28]. The

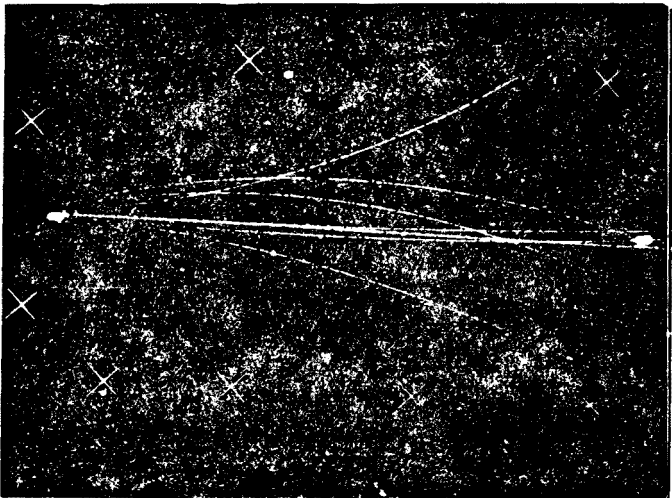


Fig. 15. Hadronic interaction as seen in a streamer chamber (Ref. [24])

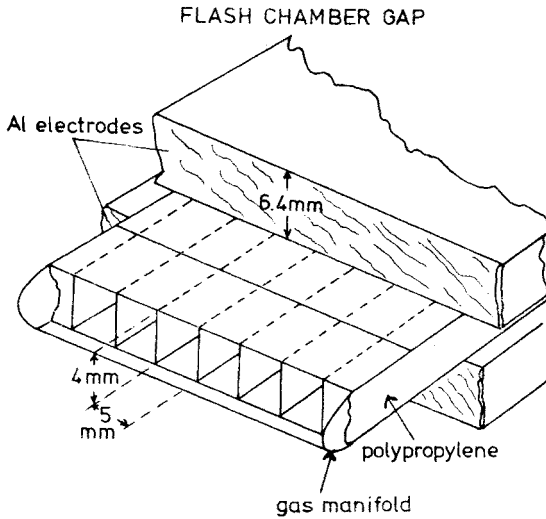


Fig. 16. Part of flash chamber made of extruded polypropylene (Ref. [28])

chamber consists of an array of rectangular tubes made of polypropylene by extrusion. This array is placed between two metal electrodes and filled with a Neon (90%) – Helium (10%) mixture (Fig. 16). A triggered HV pulse is applied on the electrodes generating a glow discharge in those cells where ionization has been induced by passing particles. This discharge can be recorded by photographing or by electronic readout. The flash chamber reaches an efficiency of 80%. Due to the extremely low cost, large volume calorimeters with fine grain sampling can be built.

II.6. Comparison of position detectors

The parameters to be compared are space and time resolution and rate of data acquisition. Table I gives typical values, where “dead time” for pulsed detectors means the time needed before a new trigger can be allowed to pulse the detector, and “sensitive time”

TABLE I

Properties of position detectors

Type	Space resolutions (μm)		Deadtime (ns)	Sens. time (ns)	Readout time (ns)	Advantages
	normal/special					
Prop. Chb.	700	100	—	50	10^3 – 10^4	time resolution
Drift Chb.	200	50	—	500	10^3 – 10^4	space resolution
Bubble Chb.	300	6	10^7	10^6	10^7	complex events
Streamer Chb.	300	30	10^6	10^3	10^7	multiple tracks
Flash Chb.	4000	2000	10^6	10^3	10^6	price

is the time during which incoming particles are registered whether they are correlated or not with the event causing the trigger. Time overlay of different events can only be avoided if the mean time interval between events is large compared to this sensitive time.

Evidently, proportional and drift chambers are best suited for precise recording at high data rates, while the pulsed bubble and streamer chambers still have the potential for optimum space resolution and multitrack analysis. The flash chamber, because of its low price and simple construction, may well find wide application in very large detectors using fine-grain calorimetry, e.g. for low-rate experiments like proton decay and neutrino experiments.

III. TIME AND IDENTITY

III.1. Photomultiplier

The main instrument for obtaining time information on a particle is the photomultiplier tube. Visible light from a scintillator liberates, by photoelectric effect, electrons from a photocathode made of alkali metals. For bialkali cathodes of Cs-K-Sb, the quantum efficiency reaches [29] a maximum of 25% around 400 nm (Fig. 17). In tubes of the linear-

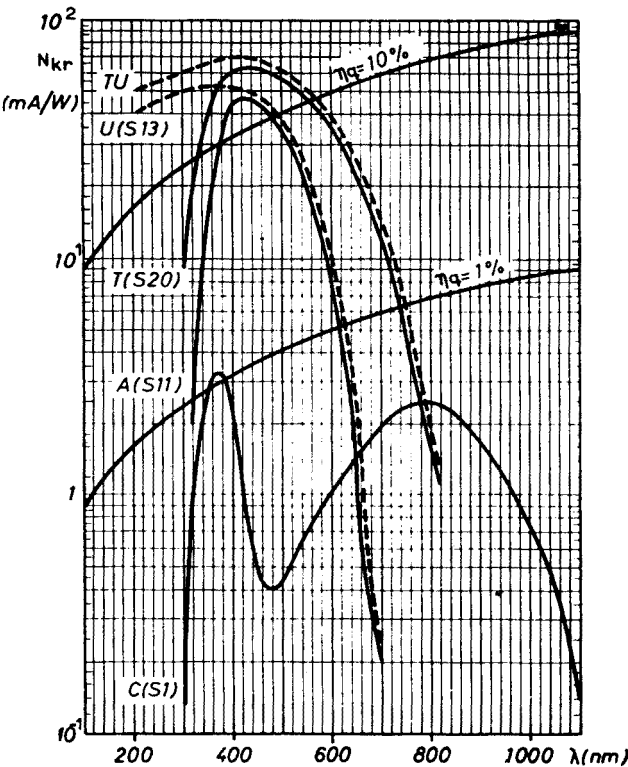


Fig. 17. Spectral sensitivity N_{kr} (mA/W) and quantum efficiency η_q (%) for photocathodes; TU and U types have quartz window, others glass window (Ref. [29])

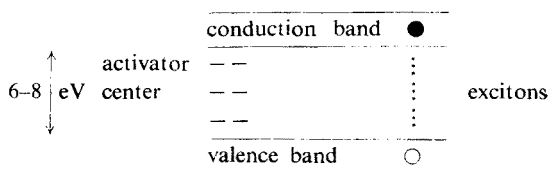
-focussing type, the photoelectrons are then focussed on the first dynode consisting of materials like BeO or Mg-O-Cs. With secondary emission yields of 3–5 per incident electron, amplifications of 10^8 for 14 dynode stages can be achieved. The risetime of the anode pulse is around 2 ns with a jitter of ~ 0.5 ns, the transit time is typically 40 ns. The price of some PM tubes has decreased in the last years because of large scale medical applications.

III.2. Scintillators

A scintillation counter has two functions: the conversion of the excitation caused by the ionizing particle into visible light and the transport of this light to the photocathode.

The mechanism of scintillation [30] is completely different for anorganic crystal scintillators and for organic crystal, liquid or polymeric scintillators.

For *anorganic crystals* doped with activator centers, the energy level diagram looks qualitatively like this:



Ionizing particles produce free electrons, free holes and excitons. These move inside the crystal until they reach an activator center A , which they transform into an excited state A^* decaying to A with emission of light. The decay time of scintillation light is then given by the lifetime of the unstable state A^* and depends on temperature like $\exp(-E_1/kT)$, where E_1 is the excitation energy. Typical data for alkali-iodides are given in Table II.

TABLE II

	NaJ(Tl)	LiJ(Eu)	CsJ(Tl)
Density (g/cm ³)	3.67	4.06	4.51
Melting point (°C)	650	450	620
Decay time (μsec)	0.2	1.3	1
Pulse height for electrons	1.0	0.35	0.28
λ_{\max} (emission) (nm)	410	470	550




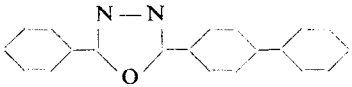
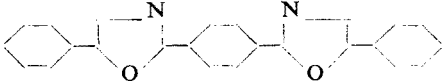
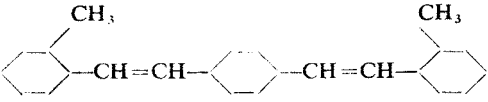
Organic scintillators, on the other hand, have very short decay times of order nano-seconds. The scintillation mechanism here is not a lattice effect, but proceeds through excitation of molecular levels which emit bands of UV light. The absorption length of this UV light in most transparent organic materials is short, of order mm, and the use of these scintillators is possible only through fluorescence excitation in a second molecule, called

wave-length shifter. The emission of this shifter material is usually chosen to be in the blue wave-length region detectable by photocathodes. These two active components in a scintillator can be solved in liquids or in a monomeric substance being polymerized subsequently. Two parameters determine the figure of merit for such a scintillator: the light yield and the absorption length in the scintillator.

Table III gives structure, wave-length of maximum emission and decay time for a few primary scintillators, as well as for two wave-length-shifters [31].

TABLE III

Scintillators and wave shifters

Primary scintillator	Structure	λ^{\max} emis. (nm)	Decay time (ns)	Yield/Yield(NaJ)
Naphtalene		348	96	0.12
Anthracene		440	30	0.5
p-Terphenyl		400	5	0.25
PBD		360	1.2	
wavelength shifter				
POPOP		420	1.6	
bis MSB		420	1.2	

For polymerizing plastic scintillator, either aromatic compounds (Styrol, Vinyltoluene) or alifatic ones (acrylic glasses, "Plexiglas") are used. The aromatic ones yield about twice as much light, but the alifatic ones are less expensive and much easier to handle mechanically.

In order to achieve a good energy resolution in large calorimeters, it is very important to obtain uniform response of a long but thin scintillator over its entire length even when the scintillator light is viewed by a photomultiplier from one end only. The observed

attenuation of light from the far end is mainly due to the absorption of the short-wavelength part of the POPOP emission spectrum, as can be seen [32] from Fig. 18. In order to obtain a more uniform response it is therefore possible to filter out the short wavelength part. The effect of a filter at 430 nm can be seen in Fig. 18: the light yield at the end of the scintillator near to the photomultiplier is diminished drastically, while the one from the far end is influenced much less.

Still, by using the filter, light is lost, and it is interesting therefore to search for an acrylic scintillator with long attenuation length and higher light yield than commercially

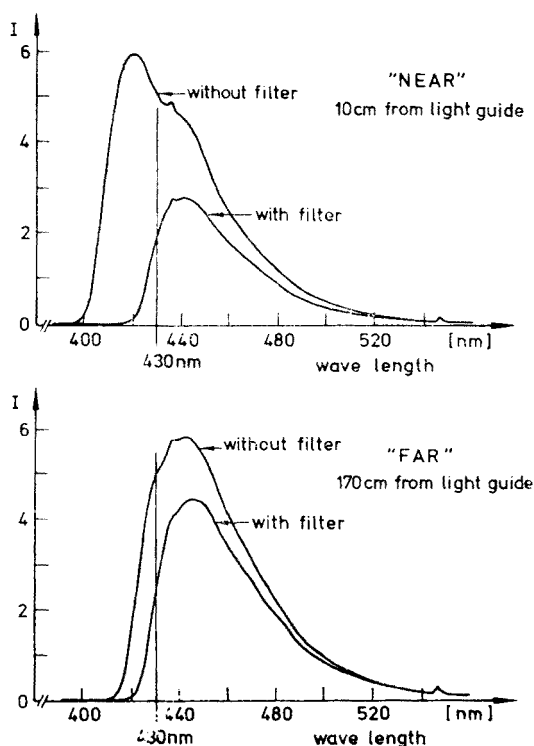


Fig. 18. Wavelength spectrum of light produced at near end or far end of scintillator (type plexiglas 1922, 180 cm long)

available. One new mixture found recently contains 3% Naphtalene, 1% PBD and 0.01% bis-MSB. The attenuation curves for a scintillator of this material with size $1800 \times 150 \times 5 \text{ mm}^3$ are shown in Fig. 19. The attenuation length with black end and filter is $\lambda = 210 \text{ cm}$, and the light yield at 160 cm from the photomultiplier side is 32% higher than the one for the commercial mixture Plexiglas 1921 (1% Naphtalene, 1% PBD, 0.01% POPOP). This new scintillator is used therefore for a new neutrino calorimeter of the CDHS group.

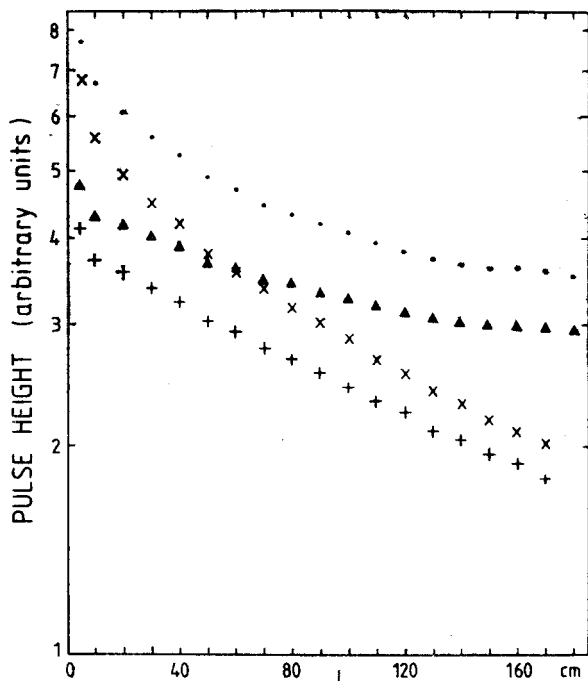


Fig. 19. Attenuation curves in a scintillator of dimensions $1800 \times 150 \times 5$ mm; (x): end blackened, (+): end blackened, yellow filter, (·): Al-reflector at end, (▲): Al-reflector and yellow filter

III.3. Light collection

The traditional way of collecting light from a scintillator is the adiabatic light guide. The (blue) scintillation light travels down the scintillator plate by multiple internal reflection. The usually rectangular radiating surface with cross-section F is imaged onto the photocathode surface f by means of bent transparent plastic rods or strips such that the radius of curvature of the rods is large compared to their thickness. In this way it can be avoided that light hits an internal surface under an angle larger than the one of total reflection. The amount of light reaching the photocathode is less than f/F due to Liouville's theorem.

An alternative method, due originally to Garwin [33], has been revived recently for applications in large-scale calorimetry [34]. The principle is shown in Fig. 20: blue light from the wavelength shifter (e.g. POPOP) leaves the scintillator and enters, through an air gap, a second shifter bar. This rod is made of acrylic material, doped with a molecule (BBQ, e.g.) absorbing the blue light and emitting isotropically green light (around 560 nm, see Fig. 21). A part of the green light is caught by the shifter bar by internal reflection and reaches the photomultipliers looking at the end of the bar. The main problems in developing this technique were (i) to find the appropriate shifting material matched to the POPOP emission spectrum and the photocathode spectral sensitivity, (ii) to find a way of optimizing the self-absorption in the green bar.

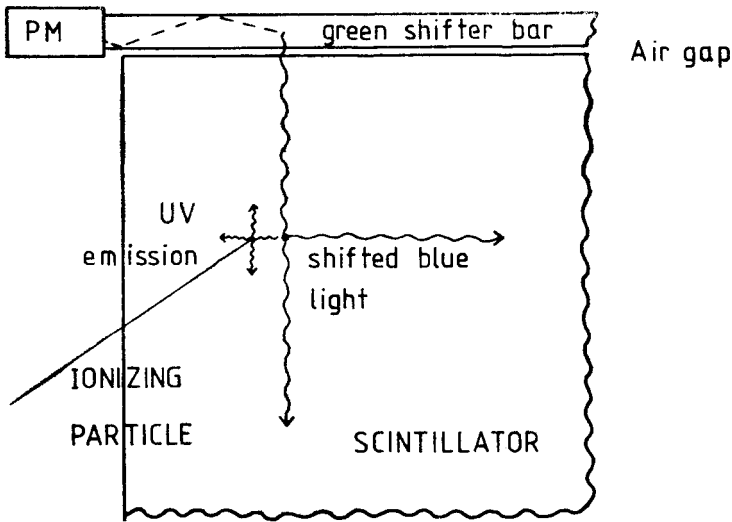


Fig. 20. Wave shifter bar technique

These problems were solved [34] by taking a 90 mg/l concentration of BBQ in Plexiglas 218. The product now is commercially available and has found wide application in large experiments.

The thickness of the green shifter bar needed for absorption of the POPOP light can be obtained from Fig. 22, where the intensity of BBQ emission has been measured [35] as a function of thickness of the green bar. An absorption length of $\lambda = (5.2 \pm 0.2)$ mm is obtained for the BBQ concentration mentioned.

The shifter bar technique can be used to collect the light from very large scintillators with a few photomultipliers. One example is the CFR neutrino calorimeter [34] with

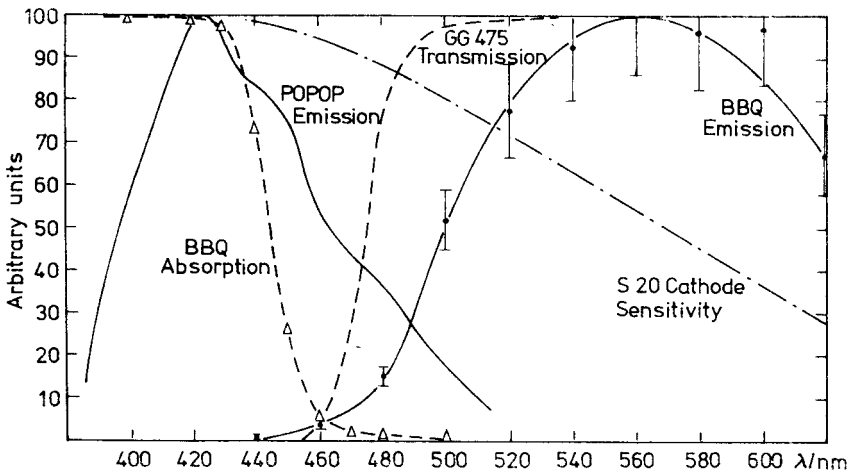


Fig. 21. Absorption and emission spectra of BBQ (Ref. [35])

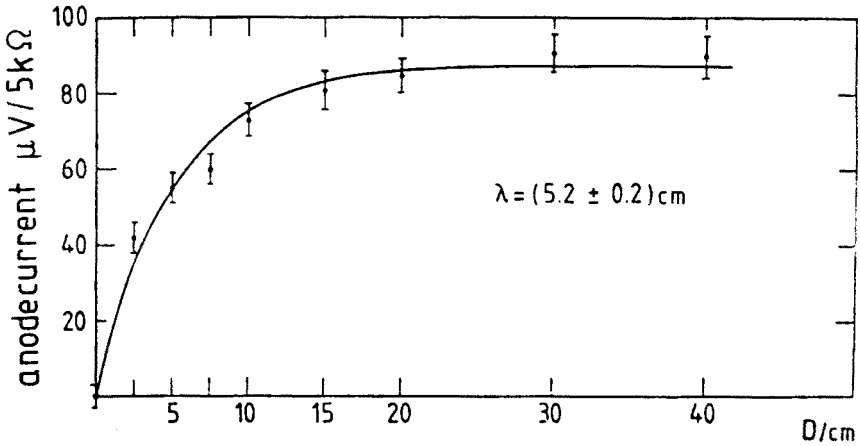


Fig. 22. Measurement of absorption length of POPOP light in BBQ (Ref. [35])

counters of 3×3 m viewed by 4 phototubes at the corners. These 4 pulseheights can be used to calculate the center of gravity of a shower of particles. Fig. 23 shows results of a measurement done with a $150 \times 300 \times 1.5$ cm³ acrylic scintillator viewed in this way. The position of a shower with 100 equivalent particles can be reconstructed with an accuracy of $\sigma \sim 8$ cm [35].

This method, therefore, has the advantage of allowing to save photomultipliers, save mechanical work for light guides and permitting a measurement of the position of a shower of particles. It does not, however, allow to disentangle several showers.

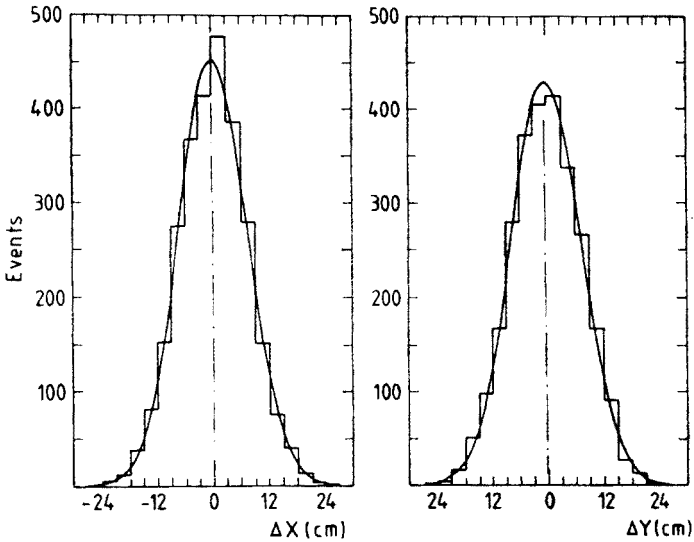


Fig. 23. Deviation of reconstructed position of a shower of 100 equiv. particles from real position; r.m.s. deviation in $\sigma_x = (7.3 \pm 0.1)$ cm, $\sigma_y = (7.6 \pm 0.1)$ cm (Ref. [35])

III.4. Time-of-flight

The identification of charged particles through their flight time between two scintillation counters requires, for momenta above 1 GeV/c, very good time resolution and quite long flight path. The time difference between two particles with masses m_1 and m_2 is for a flight path L

$$\Delta t = L/(\beta_1 c) - L/(\beta_2 c) = (L/c)(E_1 - E_2)/(cp),$$

which for $p^2 \gg m^2$ becomes $\Delta t \sim (m_1^2 - m_2^2)Lc/(2p^2)$. For π/K separation with a r.m.s. time resolution of $\sigma_t = 300$ ps, in order to obtain a $4\sigma_t$ time difference, a flight path of 3 m at 1 GeV/c and 12 m at 2 GeV/c is needed. This method of identification, as will be seen later, has the largest spatial requirements of all techniques.

III.5. Cerenkov counters

Cerenkov radiation [36] is electromagnetic radiation emitted by charged particles of velocity v traversing matter with refractive index n if $v > c/n$. The classical theory of the effect attributes this radiation to the asymmetric polarization of the medium in front of and behind the charged particle resulting in a net electric dipole moment varying with time. The radiation is emitted at an angle θ , where $\cos \theta = (ct/n)/(\beta ct) = 1/(\beta n)$. The threshold for Cerenkov-effect, $\beta > 1/n$, corresponds to a threshold in the γ factor of the particle,

$$\gamma > 1/\sqrt{1 - 1/n^2}.$$

Typical refractive indices and threshold values are given in Table IV. Unfortunately, there is a gap in the refractive indices between the gases with highest index (Pentane) and practical transparent liquids with lowest index. The development of Silica-Aerogel [37] consisting of $n(\text{SiO}_2) + 2n(\text{H}_2\text{O})$ may close this gap and permit a velocity measurement in the range of $\gamma \sim 3-5$, where the specific ionization is nearly constant.

TABLE IV

Cerenkov radiators

Material	$n-1$	γ (threshold)
Glass	0.46-0.75	1.22-1.37
Scintillator (toluene)	0.58	1.29
Plexiglas (acrylic)	0.48	1.36
Water	0.33	1.52
Aerogel	0.025-0.075	4.5-2.7
Pentane (STP)	1.7×10^{-3}	17.2
CO ₂ (STP)	4.3×10^{-4}	34.1
He (STP)	3.3×10^{-5}	123

From the relation $\cos \theta = 1/(\beta n)$ follows that the maximum Cerenkov angle becomes smaller if n approaches unity. The energy radiated per path length in the radiator is

$$\frac{dE}{ds} = \frac{4\pi^2 e^2}{c^2} \int_{\beta n > 1} \left(1 - \frac{1}{\beta^2 n^2}\right) v dv,$$

which leads to the number of photons N emitted per path length in the wavelength interval λ_1 to λ_2

$$N = \sin^2 \theta [1/\lambda_1 - 1/\lambda_2] 4\pi e^2 / hc.$$

For a detector sensitive in the visible region $\lambda_1 = 400$ nm, $\lambda_2 = 700$ nm, this corresponds to $N = 490 \sin^2 \theta$ photons/cm. Evidently, the detection of UV-light can increase this yield by a factor of 2–3.

The length of Cerenkov threshold detectors needed for separation of particles of momentum p increases as p^2 : suppose two particles with masses m_1 and $m_2 > m_1$ have to be distinguished. Then the refractive index of the radiator can be chosen such that the heavier particle with mass m_2 does not yet radiate, or is just below threshold, $\beta_2^2 \simeq 1/n^2$, and $n^2 = \gamma_2^2/(\gamma_2^2 - 1)$. Then the amount of Cerenkov light from the particle with mass m_1 is proportional to

$$\sin^2 \theta = 1 - 1/(\beta_1^2 n^2),$$

which for $\gamma \gg 1$ becomes

$$\sin^2 \theta \simeq (m_2^2 - m_1^2)/p^2.$$

In a radiator of length L , detecting photons with a quantum efficiency of 20 %, the number of photoelectrons is

$$P = 100L(m_2^2 - m_1^2)/(p^2 L_0),$$

where $L_0 = 1$ cm. In order to obtain $P = 10$ photoelectrons, a length

$$L/L_0 = p^2/((m_2^2 - m_1^2) \cdot 10)$$

is required in the optimistic case assuming that a radiator with exactly the refractive index required above can be found.

Apart from this utilization of the Cerenkov threshold, the angle of Cerenkov emission can also be measured in order to identify particles. The conical emission pattern around the radiating particle can be focussed into a ring-shaped image. An adjustable diaphragm at the focus transmits the Cerenkov light emitted in a small angular range onto a phototube. Changing the radius of the diaphragm allows a scan through regions of velocity. Differential gas Cerenkov counters correcting for chromatic dispersion in the radiator (DISC) have achieved velocity resolutions of $\Delta\beta/\beta \approx 10^{-7}$. Since the length of these counters is limited to a few meters, there is a maximum momentum at which two kinds of particles can be separated (Fig. 24). Separation of π and K mesons at several 100 GeV/c is possible with these devices. A velocity spectrum of charged hyperons in a short beam from an external proton target is shown in Fig. 25, demonstrating separation of these hyperons at 15 GeV/c momentum.

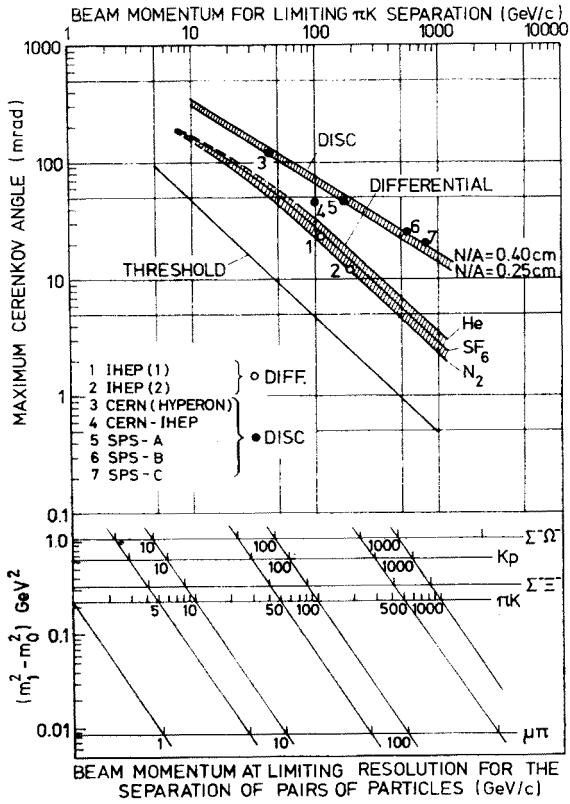


Fig. 24. Highest beam momentum for π/K separation vs maximum Cerenkov angle (Ref. [38])

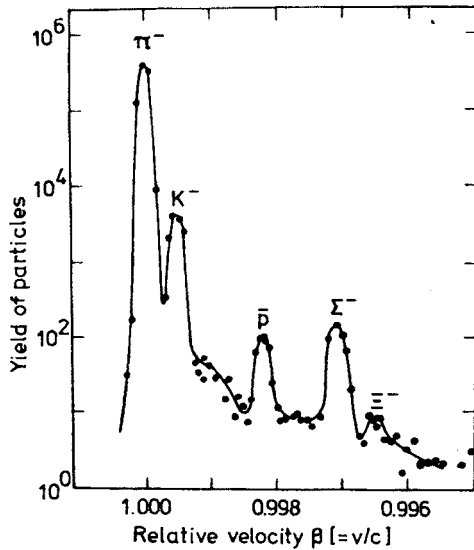


Fig. 25. Velocity distribution in a short hyperon beam selecting 15 GeV/c particles (Ref. [38])

An alternative to changing the radius of the diaphragm consists in changing the gas pressure and leaving the optical system in place. Such counters have been used in high intensity beams.

III.6. Transition radiation detectors

If a charged particle traverses a medium with varying dielectric constant, e.g. a periodic series of foils and air gaps, radiation is emitted from the interfaces between the two materials. This "transition radiation" (TR) was shown theoretically by Ginzburg and Frank [39] to depend on the γ factor of the moving particle, thus permitting an identification of particles in the very high energy region ($\gamma > 1000$) where other methods fail.

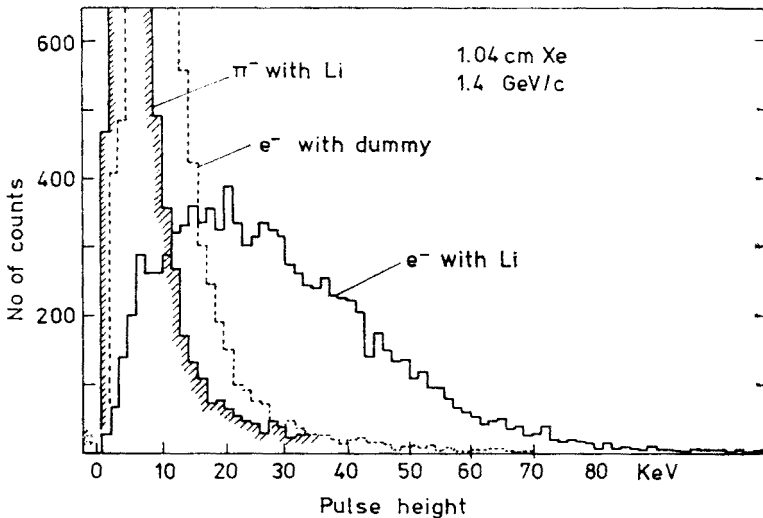


Fig. 26. Pulse height spectrum of transition radiation in Li foils detected by a Xenon proportional chamber (Ref. [1])

The intensity of this radiation is expected theoretically to have a sharp forward peak at an angle $\theta \sim 1/\gamma$ and to be proportional to γ . If a periodic sandwich of many foils is used, interference effects [40] will produce a threshold effect in γ , such that the detector can be used for discriminating between particles of different mass.

Practical applications have followed the demonstration by Garibian [41] that TR is emitted also in the X-ray region. Actual TR counters consist of a radiator followed by a proportional chamber for the detection of the X-rays emitted forward. Since the absorption of X-rays in the radiator material behaves as $Z^{3.5}$, the atomic number of the foils has to be as low as possible. In the pioneering work of Willis, Fabjan and co-workers [42] the technology of thin lithium ($Z = 3$) foils has been mastered. As a counting gas for the X-ray detector, Xenon ($Z = 54$) has been used.

The pulse height spectrum in a Xenon chamber behind 1000 Li foils of $51 \mu\text{m}$ thickness is shown in Fig. 26 together with a spectrum from a dummy radiator not producing TR. The pulseheight from TR can be clearly separated from the one from ionization loss only.

The increase of total radiated TR energy is mainly due to an increase in the average X-ray energy, as shown by the measurements in different Li/Xe-detectors [42] using electrons with $\gamma \sim 2000$ –6000. From these experiments we can conclude that (i) TR detectors at the moment can be used for $\gamma > 2000$, i.e. for electrons above 1 GeV/c and pions above 300 GeV/c. (ii) The extension of this method below $\gamma = 2000$ would require the detection of 1–5 keV X-rays and Li foils of 5 μm thickness.

Recently, Deutschmann et al. [43] have shown that the additional measurement of the angle of emission of TR photons can give a significant increase in π/K separation for $\gamma_\pi = 1000$. If 15 sets of radiators are used, each consisting of 4500 Li foils 30 μm thick with a total length of 50 cm, the pion contamination in a K meson sample of 140 GeV/c detected with 90% efficiency decreases from 20% to 4% if the angle of the TR photon is measured in addition to the charge.

III.7. Multiple ionization measurement

Between the region ($\gamma > 1000$), where transition radiation can be utilized, and the medium and low energy domain $\gamma < 100$, where Cerenkov counters and time-of-flight measurement are practical, there is a region of γ between 100 and 1000 where neither of

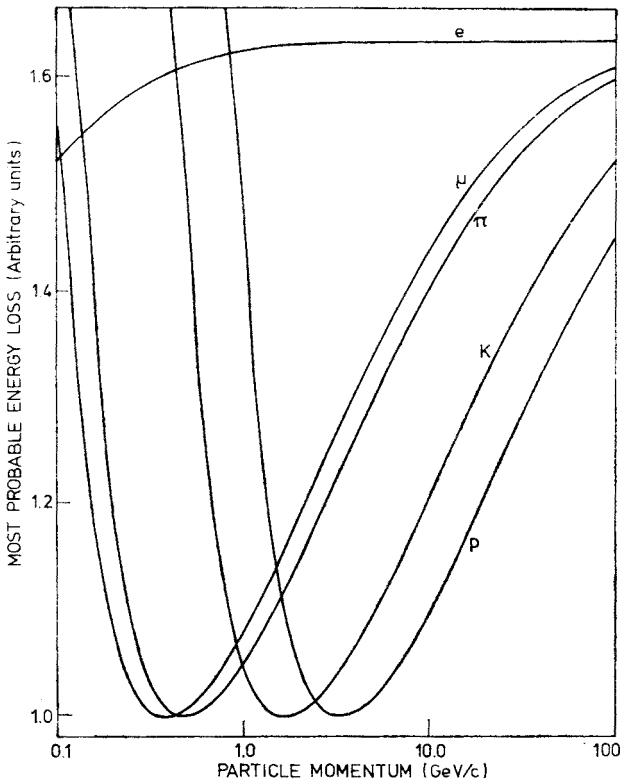


Fig. 27. Most probable energy loss in one cm of Argon (80%) Methane (20%) mixture at STP, for electrons, muons, π and K mesons and protons (Ref. [19])

these methods is applicable. Here a new kind of detector is provided by the exploitation of the relativistic rise of the ionization energy loss in this domain (see Fig. 1). In gases, this energy loss rises by a factor of 1.5, and very precise measurement is required. Because of the Landau tail from knock-on electrons, the accuracy in the determination of the mean energy loss (or alternatively the most probable energy loss) does not improve considerably by increasing the thickness of the detector. However, the resolution increases if the energy loss is measured in many consecutive thin detectors and if the large pulse-heights from knock-on electrons occurring in some of the detectors are removed. This sampling method with truncation reduces fluctuations in the mean and permits a measurement of energy loss precise enough in order to distinguish particles if their momentum is known. As can be seen from Fig. 27, the ratio of most probable energy losses of pions and kaons at 100 GeV/c is 1.05, such that π/K separation at this energy requires a resolution of less than 2%. Such resolutions can be achieved by using several hundred detectors with a total thickness of a few meters of gas. For 128 chambers, by measuring the average of the 40% smallest pulse-heights, a r.m.s. resolution of $\sigma = 2.5\%$ has been obtained for 50 GeV pions and protons [3].

III.8. Comparison of identification methods

The identification methods discussed above are usable in certain momentum domains: the time-of-flight measurement at low momenta, then threshold Cerenkov counters, DISC-Cerenkovs, multiple ionization measurement and, at ultrahigh momenta, transition radiation. The length required for π/K separation in these detectors is shown in Fig. 28. Using a typical detector length of a fixed target experiment of 30 meters and a length of 3 m for storage ring experiments, typical momentum ranges for π/K separation are calculated,

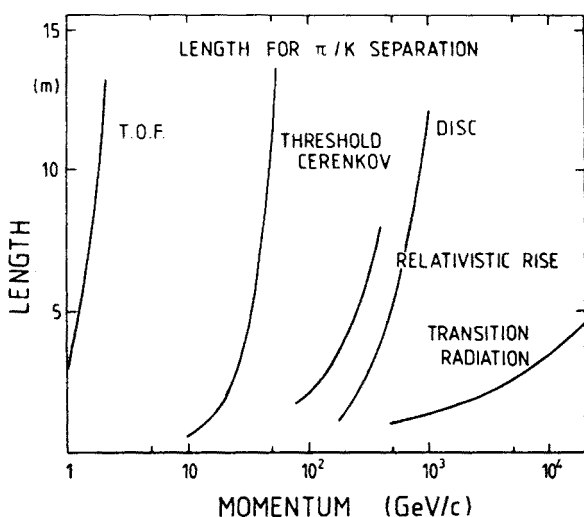


Fig. 28. Length of detectors needed for π/K separation by identification methods vs. momentum

as shown in Table V. It appears that the multiple ionization measurement is necessary for bridging the gap between threshold Čerenkov and transition radiation counters.

TABLE V

Identification methods

Method	Domain for π/K separation		Requirements
	Fixed target geometry $L = 30$ m	Storage ring geometry $L = 3$ m	
Time-of-flight	$p < 4$ GeV/c	$p < 1$ GeV/c	$\sigma_t = 300$ ps
Threshold Čerenkov	$p < 80$ GeV/c	$p < 25$ GeV/c	10 photoel.
DISC-Čerenkov	$p < 2000$ GeV/c	---	achromatic gas counter
Multiple ionization	$1.2 < p < 300$ GeV/c	$1.2 < p < 100$ GeV/c	$\sigma_E = 2.5\% \sqrt{3/L}$
Transition radiation	$\gamma > 1000$	$\gamma > 1000$	detection of > 10 keV X rays

IV. ENERGY

IV.1. Electron photon shower counters

At high energies, the ionization loss of fast ($\beta \simeq 1$) electrons is given by

$$-\left(\frac{dE}{dx}\right)_{\text{ion}} = 4\pi N_0 \frac{Z}{A} r_e^2 mc^2 [\ln(2mv^2\gamma^2/I) - 1],$$

with $r_e^2 = (e^2/mc^2)^2 \simeq (2.8 \text{ fm})^2$, while the competing loss by bremsstrahlung takes the form

$$-\left(\frac{dE}{dx}\right)_{\text{brem}} = E \frac{4N_0 Z^2 r_e^2}{137A} \ln \frac{183}{Z^{1/3}} =: \frac{E}{X_0},$$

where the “radiation length” X_0 is defined this way, and m is the electron mass.

While ionization dominates at low energies, bremsstrahlung takes over at high energies, and the ratio R of bremsstrahlung loss and ionization loss comes out to be $R \simeq ZE/600$, where E is measured in MeV. The energy at which this ratio becomes unity, the “critical energy” E_c therefore has the approximate value $E_c \sim 600/Z$ MeV which for lead is $E_c = 7.3$ MeV.

For $E \gg E_c$, bremsstrahlung dominates and the exponential decrease of the energy is given by the radiation length $E \sim \exp(-x/X_0)$.

The interaction of photons at high energy is also governed by the radiation length: the cross-section for pair creation

$$\sigma_{\text{pair}} = 4Z^2 r_e^2 / 137 \left[\frac{7}{9} \ln \frac{183}{Z^{1/3}} - \frac{1}{54} \right]$$

gives a probability P for pair creation in one radiation length

$$P = \sigma_{\text{pair}} \cdot \frac{Nq}{A} \cdot \frac{X_0}{q} = \frac{7}{9}.$$

Table VI gives radiation length and critical energy for some materials [44].

TABLE VI

Radiation length and critical energy

Material	$X_0[\text{g}/\text{cm}^2]$	$E_c[\text{MeV}]$
H_2	63	340
Al	24	47
Fe	13.8	24
Pb	6.3	6.9
Leadglass SF 5	10.2	~ 16
Plexiglas	40.5	80
H_2O	36	93
NaJ (Tl)	9.5	12.5

The interaction of a high-energy photon or electron therefore leads to a cascade of electrons and photons; starting with a photon of energy E_0 , after $1X_0$ we have 2 particles each of energy $E_0/2$, after nX_0 there are 2^n particles of energy $E_0/2^n$. The cascade stops approximately when the particles approach the critical energy, i.e. if $E_0/2^n = E_c$.

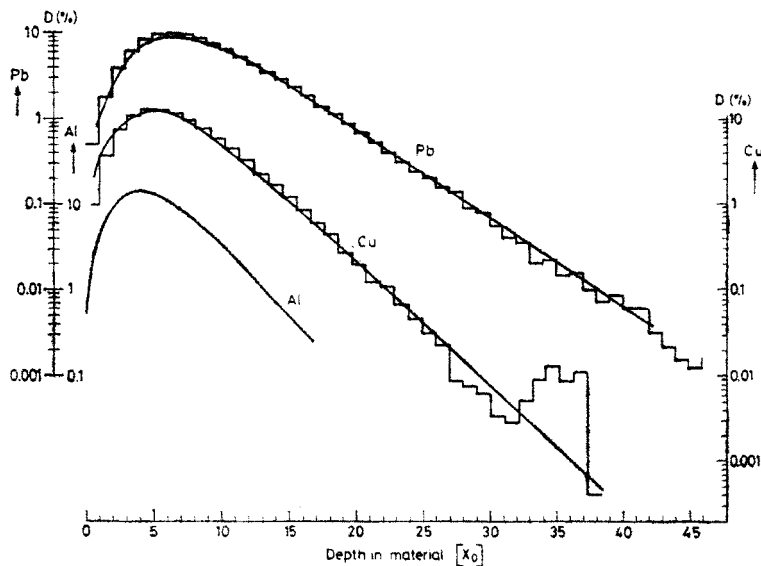


Fig. 29. Longitudinal distribution of energy deposition in a 6 GeV electron shower; measurements (line) and Monte Carlo calculation (histogram) (Ref. [45])

The number of generations up to the maximum therefore is $n = \ln(E_0/E_c)/\ln 2$, and the number of particles at the maximum $N_p = 2n = E_0/E_c$. The total integral path length S of all electrons or positrons in the shower is:

$$S = \frac{2}{3} \cdot X_0 \sum_{v=1}^n 2^v + s_0 \frac{2}{3} N_p = \left(\frac{4}{3} X_0 + \frac{2}{3} s_0\right) E_0/E_c,$$

where s_0 is the path length of electrons below the critical energy.

The path length S is proportional to the total energy E_0 . More refined Monte Carlo calculations give the same properties of electron-photon showers:

- (i) the number of particles at maximum N_p is proportional to the primary energy E_0 ,
- (ii) the total track length of electrons and positrons S is proportional to E_0 ,
- (iii) the depth at which the maximum occurs X_{\max} increases logarithmically: $X_{\max}/X_0 = \ln(E_0/E_c) - 1$.

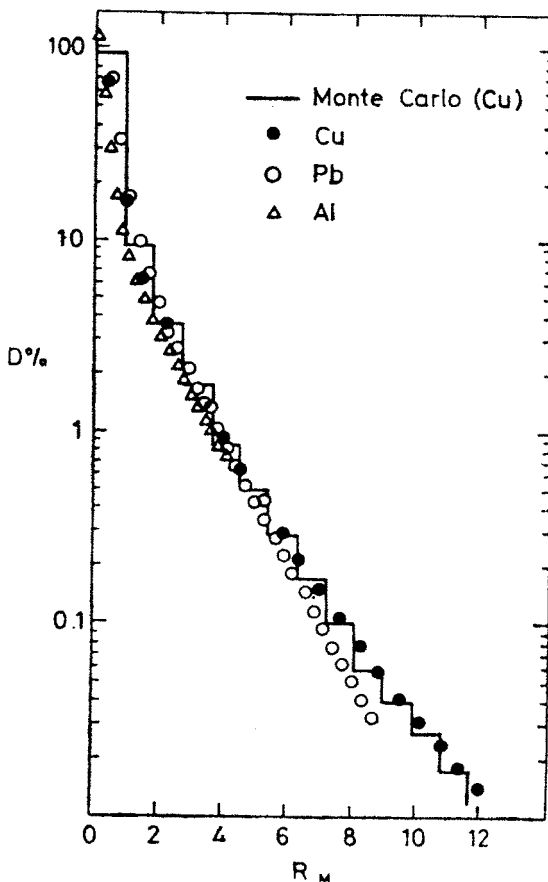


Fig. 30. Transverse distribution of energy deposition in a 6 GeV electron shower; data: points; Monte Carlo: histogram; $R_M = 21 \text{ MeV} \cdot X_0/E_c$ is the Molière unit (Ref. [45])

The longitudinal energy deposition in an electromagnetic shower can be seen in Fig. 29 as measured [45] for 6 GeV electrons. The transverse dimension of a shower is determined by the multiple scattering of low energy electrons. It turns out that a useful unit for transverse shower distributions is the Molière unit $R_M = 21 \text{ MeV} \cdot X_0/E_c$. As shown by the measurements [45] in Fig. 30, the distribution of shower energy in transverse (radial) bins scaled in R_M is independent of the material used, and 99% of the energy are inside the radius of $3 R_M$.

Electromagnetic shower counters detect the electrons and positrons in the shower and measure their integrated path length. This is done by detecting either their ionization energy loss by scintillation counters or their Cerenkov radiation emission. Two kinds of scintillation counters are in use:

(i) the NaJ crystal, where blocks of $15 X_0 = 40 \text{ cm}$ length and a diameter $D = 3 R_M \approx 13 \text{ cm}$ are viewed by one photomultiplier; energy resolutions of 1% at 10 GeV are typical.

(ii) lead-scintillator sandwiches, where the path length of electrons is sampled in the scintillator plates; the resolution $\sigma(E)$ here is mainly due to statistical fluctuations ("sampling fluctuation") and therefore decreases with increasing energy E

$$\sigma(E)/E \sim 5\%/\sqrt{E(\text{GeV})}$$

is achieved typically.

The detection of Cerenkov light is done conveniently in transparent lead glass blocks. This material, with a radiation length of 2.5 cm, can again be shaped in cells of appropriate size. Cerenkov light emitted by the electrons is trapped in the block (refractive index $n = 1.7$) and registered by a photomultiplier. Resolutions of

$$\sigma(E)/E \sim 5\%/\sqrt{E(\text{GeV})}$$

are the standard.

IV.2. Hadron calorimeters

The scale for the spatial development of a hadronic shower, the inelastic production of secondary hadrons, which again interact inelastically producing tertiary hadrons, and so on, is given by the nuclear absorption length λ . From the inelastic cross-section σ , $\lambda = A/(\sigma N_0 \varrho)$ can be obtained. The experimental values of λ for materials usable for calorimetry are 77 g/cm²(C), 135 g/cm²(Fe), 210 g/cm²(Pb) and 227 g/cm²(U). Compared to the small values for radiation length for high Z materials enabling the construction of correspondingly small shower counters, the size of hadronic showers is large, typical values for Fe calorimeters are 2 meters depth and 0.5 m transverse size. The need for such sizes is demonstrated by the measurements [46] on the longitudinal shower development shown in Fig. 31, where the center of gravity, the length for 95% energy containment and the length, where the average particle number goes below one ("shower length") are displayed as a function of incident pion energy for a 5 cm Fe sampling calorimeter. In a similar way, Fig. 32 gives lateral shower sizes for 95% energy containment.

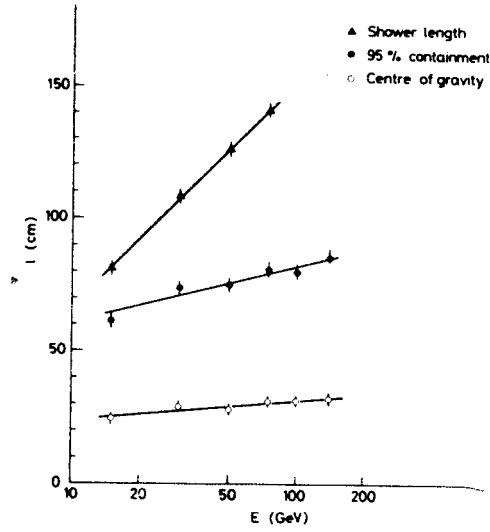


Fig. 31. Shower center of gravity in iron, length for 95 % energy containment and length where average particle number goes below one as function of pion energy (Ref. [46])

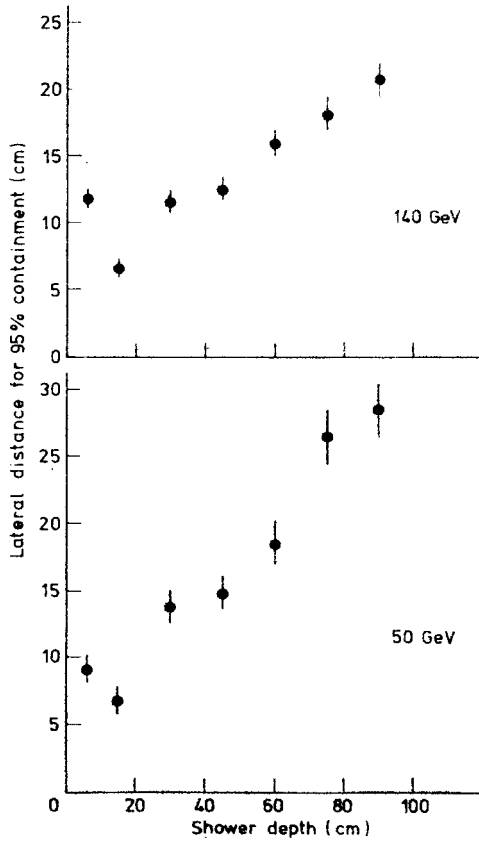


Fig. 32. Lateral dimension for 95 % energy containment as a function of depth in iron (Ref. [46])

In addition the energy seen in a sampling calorimeter for hadrons is incomplete for several reasons:

(i) there are particles escaping the calorimeter carrying away energy, like muons and neutrinos from pion decay and neutrons,

(ii) there is nuclear excitation and breakup resulting in low energy γ rays or heavy fragments, which do not reach the sensitive part of the sandwich.

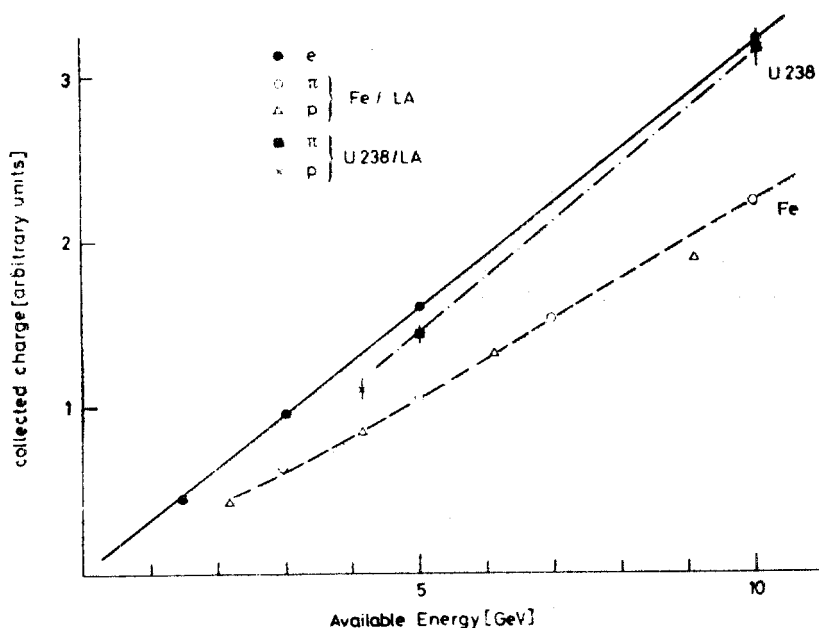


Fig. 33. Detected energy deposition in sampling calorimeters of Fe and U for electrons, pions and protons vs particle energy (Ref. [47])

This loss of visible energy is typically 30%, as can be seen by comparing the light collected from electron- and hadron-induced showers (Fig. 33). Since in a hadronic shower the electromagnetic component can occasionally be dominant through energetic π^0 production, this loss induces a fluctuation in response which contributes significantly to the resolution.

On top of this fluctuation there is the sampling fluctuation which gives rise to a resolution about twice as large as electromagnetic showers (see IV. 1). However, the effects of the fluctuation in energy leakage and in the electromagnetic component of the hadronic shower are much larger here and lead to energy resolutions of about

$$\sigma(E)/E \sim (0.9-0.5)/\sqrt{E(\text{GeV})},$$

if the thickness of material between the sampling devices ("sampling thickness") is below 5 cm of iron.

Two ways of improving this resolution have been invented and tried out successfully:

(i) The loss of visible energy through the nuclear excitation and breakup mechanism can be nearly completely compensated by the energy release in nuclear fission of ^{238}U . Energetic photons from the fission contribute to the observed signal such that the pulse-height for hadron showers becomes nearly equal to the one of electromagnetic showers, as shown [47] in Fig. 33. The corresponding fluctuations disappear, and the energy resolution decreases by about a factor of two. Experimental results are shown in Fig. 34, they correspond to

$$\sigma(E)/E = 0.3/\sqrt{E(\text{GeV})}$$

which is only 50% higher than the lower limit given by sampling fluctuations.

(ii) Another method [48, 49] reduces the fluctuation due to the electromagnetic component by weighting the response of individual counters. Electromagnetic parts of the shower are localized producing very large depositions in individual counters. If the measured response in one counter E_k is corrected downwards for large responses, $E'_k = E_k(1 - CE_k)$, then the resulting resolution in the sum $\sum E'_k$ is markedly improved over the one in $\sum E_k$, as shown [49] in Fig. 35 for a 2.5 cm Fe sampling calorimeter exposed to 140 GeV/c pions. The resolution displayed in Fig. 34 can be approximately described by

$$\sigma(E)/E = 0.58/\sqrt{E(\text{GeV})}$$

between 10 and 140 GeV/c.

If the sampling thickness is larger, the sampling fluctuations increase and the resolution σ/E increases with d ; Fig. 36 gives some measurements [49].

The sampling of ionization in hadron calorimeters can be done by scintillators, liquid argon ionization chambers, proportional chambers, or flash tubes. The choice between

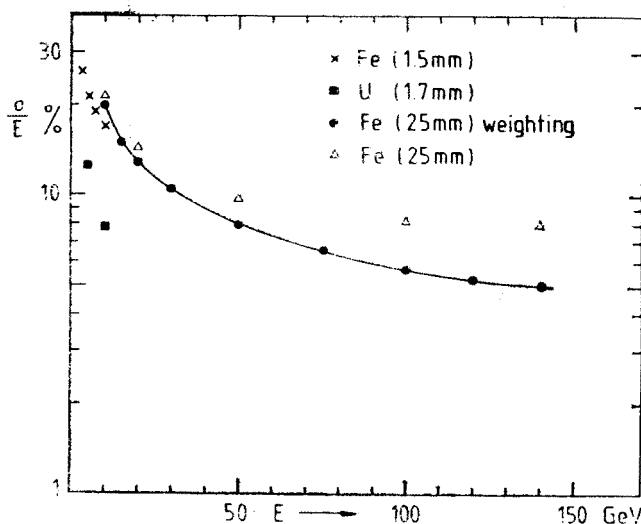


Fig. 34. r.m.s. energy resolutions obtained with hadronic sampling calorimeters; Fe(1.5 mm) and U(1.7 mm): Ref. [47]; Fe(25 mm): Refs. [46] and [49]

these detectors depends on the desired resolution, granularity and cost. For moderate-sized geometries, liquid argon and scintillators are used for best resolution. For very large fine grain calorimeters (ve scattering, proton decay), the proportional tubes or flash tubes give granularities down to $5\text{ mm} \times 5\text{ mm}$ at a price which still allows the construction of multi-hundred ton experiments.

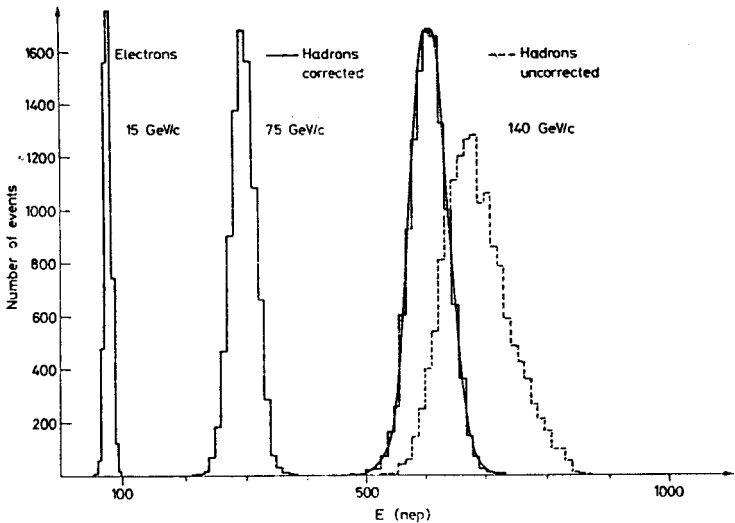


Fig. 35. Pulse height spectra (in n.e.p.) for electrons and hadrons in a 2.5 cm Fe sampling calorimeter (Ref. [49])

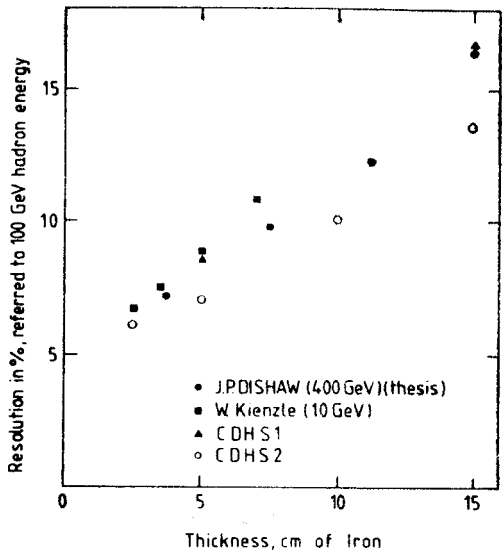


Fig. 36. r.m.s. hadronic energy resolution for ion calorimeters with different sampling thickness; J. P.Dishaw (Ref. [48]); CDHS 1 (Ref. [46]); CDHS 2 (Ref. [49])

IV. 3. Monitoring of calorimeters

In a typical large-scale calorimeter there will be several thousand channels of analog pulseheight information which is converted to digits and registered. A severe problem with such a number of channels is their calibration and monitoring.

The calibration can be done by using suitable hadron beams and calibrating the response of the calorimeter, where for each sampling detector the pulseheight is measured in terms of minimum ionization deposited by high energy muons.

If there are not as many muons in each sampling detector as are needed for day-to-day monitoring, another source of calibrated pulseheights is needed. For liquid argon calorimeters, such a source is obtained by depositing a known amount of charge into the ion chamber. The same can be done for proportional chambers.

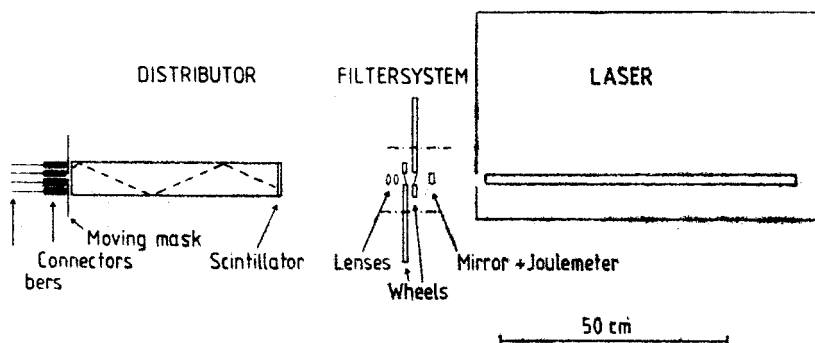


Fig. 37. Dortmund Laser calibration system (Ref. [51])

For scintillation counters, a novel kind of monitoring systems is under construction now [50, 51]. The light source here is a pulsed Nitrogen laser emitting at 337 nm. There are different schemes of distributing the light onto a few thousand counters.

In one of the systems [50], built for the UA 1 experiment, the laser light is injected into a rectangular box covered inside with a highly reflecting material (Millipore). After many reflections inside the light is diffused and leaves the box through Quartz fibers of 200 μm diameter. This fiber has attenuations of ~ 400 db/km in the UV. Each of the 8000 fibers is connected to a plexiglas prism glued to the center of the scintillator. The UV light pulse then produces scintillation light which reaches the PM photomultiplier and produces a digital pulseheight.

In another system [51], designed for the improved CDHS detector, the laser beam passes through a filter, is widened up optically, and then illuminates a scintillator piece glued onto a plexiglas rod (Fig. 37). The blue POPOP light emitted isotropically from the scintillator travels down the rod by internal reflection and is partially accepted by the 2304 fibers grouped into 12 bundles of 192, each bundle in one connector. The homogeneity of illumination of the fibers is within 1%. A mechanical mask moving across in front of the connectors permits one bundle at a time to be illuminated. This is required by the number of ADC channels available. The transmission of the fibers of 200 μm diameter

(QSF 200 A) is 180 db/km for the blue scintillator light, such that over a length of 25 m the attenuation is a factor of 2.8. Each fiber is connected to a light guide through a small (4 mm dia.) cylindrical rod. With this system, by exchanging filters of different density on a "filter wheel", the linearity of all tubes can be measured in a dynamic range from 1 to 2000 times minimum ionization. The absolute calibration is done by comparing one of the fiber outputs to the standard light from an α source embedded in a scintillator.

V. MOMENTUM

V.1. Magnet shapes for fixed target experiments

In a fixed target interaction, the reaction products are usually concentrated in a cone around the incident beam direction (z), because of their limited transverse momenta and the Lorentz boost for longitudinal momenta. If such a particle with momentum (P_x, P_y, P_z) traverses a homogeneous magnetic field ($0, B_y, 0$), it receives a transverse momentum kick

$$\Delta P_x = -e \int B_y dz$$

which gives for a field integral of 10 kG · m a transverse momentum change of 0.3 GeV/ c . The corresponding deflection of the particle is inversely proportional to its momentum, and a measurement of the projected angles in the (x, z) plane yields in the simplest approximation the momentum

$$P = e \int B_y dz / (\sin \theta_{in} - \sin \theta_{out}).$$

If the magnetized volume is evacuated and the multiple scattering in the position detectors is neglected, the error in momentum, δP , comes from measurement error δx in the chambers alone

$$\delta P/P = 2(P/\Delta p_x)(\delta x/L),$$

if the lever arm for the angle measurement before and after the magnet is L . For a field integral of 50 kGm, $\delta x = 0.3$ mm and $L = 3$ m this gives $\delta P/P \sim 1.3\%$ at 100 GeV/ c .

These "air core" magnets come in different forms (Fig. 38): H-magnets have symmetrical flux return yokes, C-magnets asymmetrical ones (and a less uniform field). The amount of iron in the flux return depends on the desired field strength in the air gap. For a cubic magnetized region, the volume of iron needed, V_{Fe} , relative to the magnetized air gap volume V_{Air} for different field strength B in the gap is shown in Fig. 39. If B has to reach the saturation field strength B_s , then $V_{Fe}/V_{Air} \sim 3$, which is very uneconomical. More usual magnets have $B/B_s \sim 1/2$ to $1/3$.

If the particles to be analyzed are high-energy muons, a more economical form of magnets are "iron core" magnets (ICM). Here the field lines stay completely within iron, either in the form of a toroid, where the field lines are circular around a central hole for the coils, or in a kind of H-magnet, where the central region is also filled with iron (Fig. 38). The momentum resolution here is limited by multiple scattering of the muons

in iron and the measurement error of the muon track. Multiple scattering results in a transverse momentum change of

$$\Delta p_T^{\text{MS}} = 21 \text{ MeV}/c \sqrt{L/X_0}.$$

The momentum resolution is given by ratio $\Delta p_T^{\text{MS}}/p_T$ and is therefore independent of the momentum. The resolution improves with the length of the ICM as \sqrt{L} , and is 12% at $L \sim 5 \text{ m}$ if the position measurement error is smaller than the error by multiple scattering.

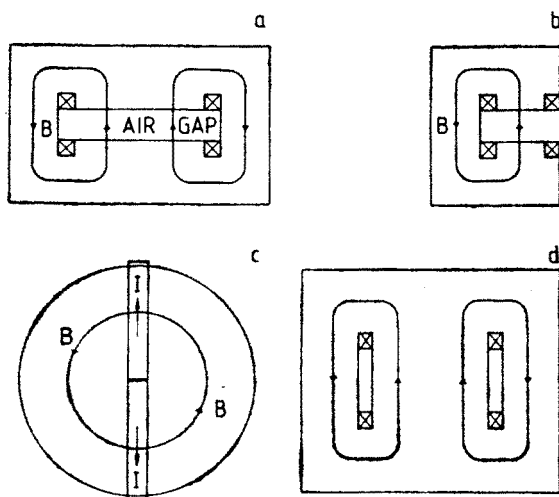


Fig. 38. Magnet shapes for fixed target experiments a) H-magnet, b) C-magnet, c) toroidal ion core magnet, d) H-type iron core magnet

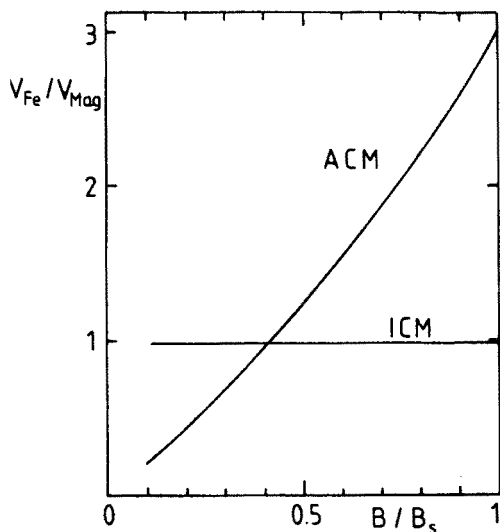


Fig. 39. Volume of iron V_{Fe} needed per magnetized volume used in experiment for iron core magnets (ICM) and air core magnets (ACM) vs. magnetic flux density B in units of saturation density B_s

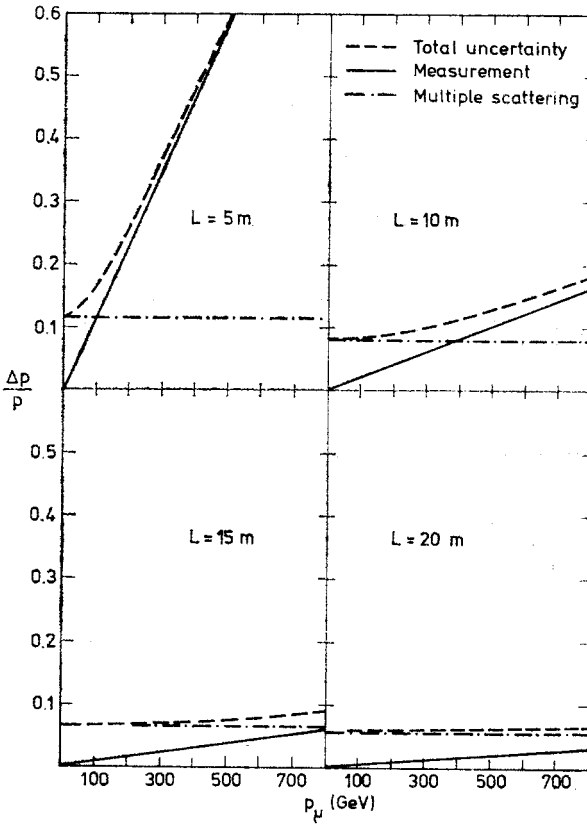


Fig. 40. Momentum resolution for iron core magnets for different iron length, L . Contributions from measurements and multiple scattering are given separately

For high momenta ($P > 100 \text{ GeV}/c$) this is not the case, since the momentum resolution from measurement error increases linearly with momentum. For a position error of 1 mm in drift chambers after every 75 cm of iron, $(\Delta P/P)_{\text{meas}} \sim 12\%$ at 100 GeV/c, equal to the error by multiple scattering. The error $(\Delta P/P)_{\text{meas}}$ decreases with a $5/2$ power of the magnet length L , because not only the bending power and the lever arm increase with L , but also the number of measurements along the track. Fig. 40 gives these two contributions to the momentum resolution for different length of iron core magnets.

V.2. Magnet shapes for storage ring experiments

Interaction rates in colliding beam experiments are notoriously low, and 4π solid angle coverage is very desirable. Various magnet geometries are imaginable (Fig. 41).

(i) Dipole magnet with two compensators to keep particles in orbit: uniform field, good analyzing power in the forward/backward direction, bad analyzing power for particles emitted parallel to the field lines; synchrotron radiation of the beams is prohibitive for e^+e^- rings.

(ii) Split-field dipole magnet: good resolution in the forward direction, very inhomogeneous field at 90° , complicated track fitting procedure; synchrotron radiation in e^+e^- rings; being used at the ISR.

(iii) Toroid: the inner current sheet or copper bars have to be crossed by particles before momentum analysis, momentum resolution is affected for low energy particles, advantage: no field in beam region.

(iv) Solenoid: no force on beam particles, good analyzing power for particles emitted at 90° ; access to inner detector only through end caps.

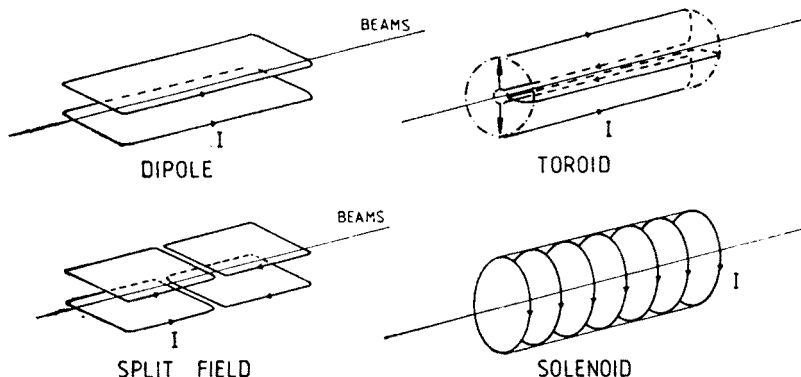


Fig. 41. Magnet shapes for storage ring experiments; lines are currents

For proton (and antiproton) storage rings, split-field and dipole magnets are being used as well as solenoids, while for electron-positron rings the solenoid has been most widely chosen. In general, storage ring detectors resemble each other much more closely than the detectors at fixed target machines.

VI. REALIZATION OF DETECTOR SYSTEMS

Detectors of the kind described in the foregoing chapters are assembled for specific experiments which nowadays reach big dimensions (~ 50 m length), large mass (up to 2000 tons) and huge complexity (up to 10^5 channels of analog and digital information). It is evident that the variety and versatility of experiments at fixed target proton machines is much larger than at electron-positron storage rings, because there are so many more variations in experimental conditions possible: different incident particles, different targets, different energies, different interactions (weak, electromagnetic, strong). In spite of this, the contribution of electron-positron rings (SPEAR, DORIS, PETRA, Cornell and PEP) has been important in the last 6 years. This evolution may continue with the proton-antiproton collider at CERN in 1981 and FNAL in 1984, Isabelle at Brookhaven, the Large Electron Positron Machine (LEP) at CERN and the Electron Proton Projects at DESY (HERA) and at FNAL.

Out of the large number of detector systems in use or being built presently, I have chosen three examples.

VI.1. A hadron beam detector

This experiment (NA 5 at CERN [52]) uses a hybrid detector (Fig. 42). A hadron beam from the SPS impinges on a hydrogen target, imbedded in a large dipole magnet. Particles from the interaction vertex are bent by the field and analyzed in a streamer chamber. Large multiplicities of charged particles do not hinder the performance of the chamber

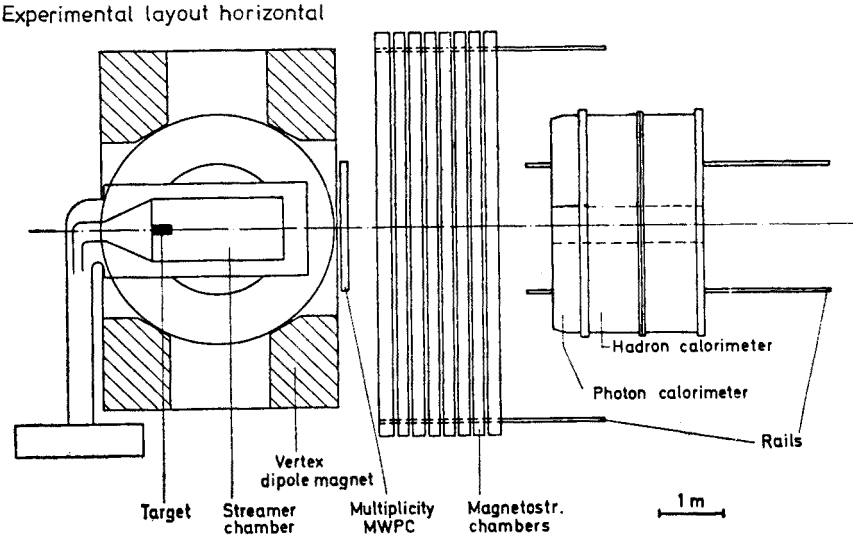


Fig. 42. Experimental layout of NA 5 hadron experiment (Ref. [52])

(see Fig. 15). The momentum measurement is further improved by the eight large (6 m wide) magnetostrictive spark chambers. A trigger on jets and their analysis is made possible by the hadron calorimeter [53], whose angular range can be changed by moving it back and forth on rails. The experiment searches for jet structure in hadron-hadron reactions at high transverse momentum.

VI.2. A neutrino detector

Since the neutrino nucleon total cross-section is only 10^{-36} cm^2 at 100 GeV neutrino energy, neutrino detectors have to be massive. This detector (Fig. 43) of the CERN-Dortmund-Heidelberg-Saclay-Collaboration [18] uses the target weight of 1500 tons of iron, arranged in circular plates of 3.75 m diameter, for three other functions:

- (i) 75 cm of iron thickness are combined to form a toroidal magnet,
- (ii) between the iron slabs of 5 cm (for 7 magnets) or 15 cm (for 8 magnets) 8 scintillators viewed by 16 photomultipliers sample the ionization energy deposited by hadronic showers,
- (iii) the range in iron enables identification of muons.

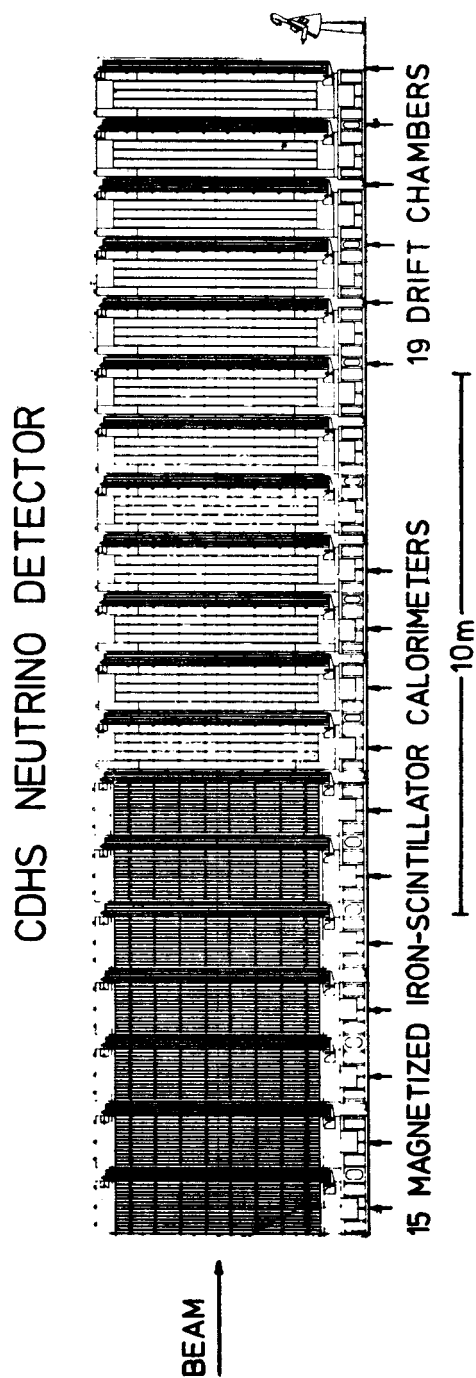


Fig. 43. Experimental layout of CDHS neutrino experiment (Ref. [18])

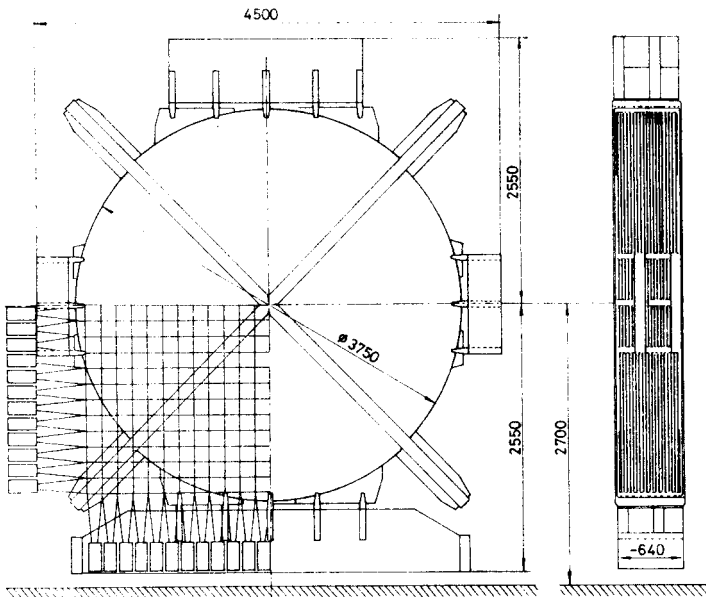


Fig. 44. New toroidal magnetic calorimeter of CDHSW collaboration

Between two magnets, driftchambers [18] with 3 planes of wires strung in 120° sequence measure the muon momentum to about 10%. The detector has recorded so far about 3×10^6 neutrino interactions, with zero, one, two, three and four muons. For experiments at higher energy at CERN and at Fermilab, a part of the detector is being rebuilt (Fig. 44) with 2.5 cm iron plates and a finer scintillator mesh (15 cm wide strips in both directions).

VI.3. A storage ring detector

For the proton-antiproton collider at CERN, one of the detectors is the UA 1 experiment [54]. Fig. 45 shows a sketch of this enormous apparatus: a dipole field configuration with two compensator magnets was chosen. The central detector uses image readout similar to the TPC, but in a different geometry, because the magnetic field lines are perpendicular to the beam direction. The E and B fields are not parallel here, such that the improvement on diffusion broadening during drifting does not apply, and a drift space of 20 cm is used. From about 10000 wires pulseheights and time information is read out to get a spatial rms resolution of $250 \mu\text{m}$ and a dE/dx measurement. The central detector (radius 1.2 m, length 5.7 m) is surrounded by an electromagnetic calorimeter inside the magnetic field and by the hadronic calorimeter embedded in the pole pieces of the dipole magnet. The wavelength shifting technique is used for the light collection from the 8000 scintillators. The detector is covered on three sides by muon detectors (Fig. 46).

If the particle multiplicity in hadron-hadron collisions continues to rise logarithmically up to 560 GeV center-of-mass energy, then the typical number of secondaries will be

EXPERIMENTAL AREA FOR $p\bar{p}$ IN LONG STRAIGHT SECTION 5 OF THE SPS

— Vertical section in beam direction.

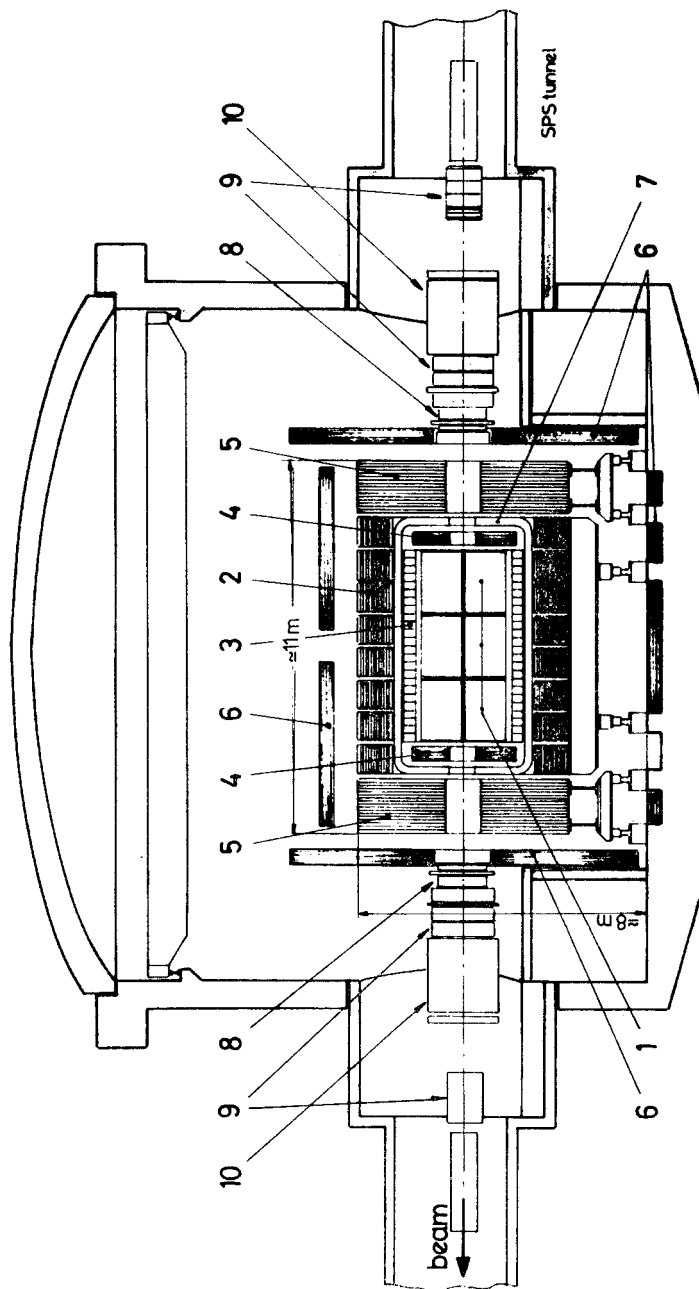


Fig. 45. Side view of UA 1 detector at antiproton-proton collider (Ref. [54]): 1 — central detector with image readout, 2 — large angle calorimeter and magnet yoke, 3 — large angle shower counter, 4 — end cap calorimeter, 5 — end cap calorimeter, 6 — muon detector, 7 — aluminium coil, 8 — forward shower counters and calorimeters, 9 — forward shower counters and calorimeters, 10 — compensator magnet

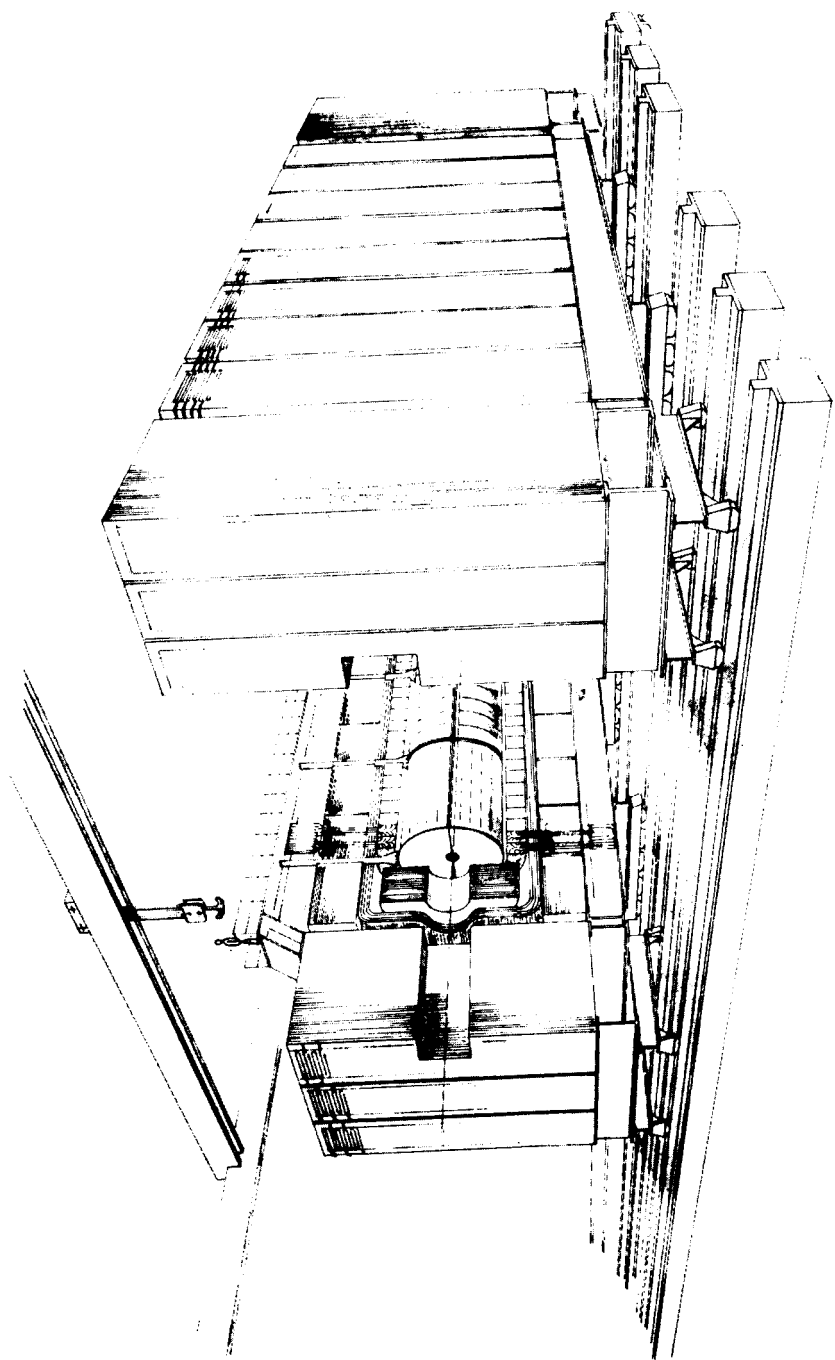


Fig. 46. Perspective view of UA 1 detector (Ref. [54])

around 50. Each of the events recorded by this detector will contain more than 10^5 bits of information. On-line data reduction will become important for this enormous mass of information.

CONCLUSION

A lot of progress in detector technology has been achieved over the last years, and the discoveries during this exciting time of particle physics would not have been possible without it. Developments will go on: the precision in position measurement may still improve using the center-of-gravity method, a reduction in size of electromagnetic calorimeters may be possible if the new kind of crystal scintillators based on Bismuth instead of Iodine [55] can be produced at reasonable cost, and data processing will still become faster and more efficient by using microprocessors and specialized 32-bit processors.

It will be necessary and possible to construct for the new generation of accelerators and storage rings general purpose detector systems of the enormous size and complexity of, e.g., the UA 1 experiment. These experiments require large experimental teams for construction, maintenance, running and data analysis. It is an open question whether this is an unavoidable consequence of these accelerators and storage rings, or if there is still a reasonable chance for smaller specialized experiments to contribute significantly to the progress in elementary particle physics.

This question is important because the vitality of physics in this field depends, amongst other factors, on the chance which young physicist see to make an individual identifiable contribution in such large collaborations.

It is a great pleasure to thank Professor Andrzej Białas for the hospitality extended to me and for the friendly atmosphere at the XXth Zakopane School of theoretical physics.

REFERENCES

- [1] C. W. Fabjan, H. C. Fischer, CERN preprint EP/80-27 (1980), to be published in *Reports on Progress in Physics*.
- [2] H. A. Bethe, *Hdb. Physik* **24**, 518 (1933); R. M. Sternheimer, R. F. Peierls, *Phys. Rev.* **B3**, 3081 (1971).
- [3] I. Lehraus et al., *Nucl. Instrum. Methods* **153**, 347 (1978).
- [4] L. D. Landau, *J. Exp. Phys. (USSR)* **8**, 201 (1944).
- [5] G. Charpak, *Ann. Rev. Nucl. Sci.* **20**, 195 (1970).
- [6] G. Charpak et al., *Nucl. Instrum. Methods* **62**, 235 (1968); *ibid.* **80**, 13 (1970).
- [7] L. B. Loeb, *Basic Processes of Gaseous Electronics*, U. of Calif. Press, Berkeley 1961.
- [8] H. G. Fischer et al., Proc. Int. Meeting on Prop. and Drift Chambers, Dubna 1975, (JINR) report D 13-9164.
- [9] P. Schilly et al., *Nucl. Instrum. Methods* **91**, 221 (1971).
- [10] W. Cunitz et al., *Nucl. Instrum. Methods* **91**, 211 (1971).
- [11] T. Trippe, CERN NP Int. Report 69-18 (1969).
- [12] K. Kleinknecht et al., CERN NP Int. Report 70-18 (1970).
- [13] V. Radeky, *IEEE Trans. Nucl. Sci.* **NS-21**, 51 (1974).
- [14] G. Charpak et al., *Nucl. Instrum. Methods* **148**, 471 (1978).
- [15] G. Charpak et al., *Nucl. Instrum. Methods* **80**, 13 (1970).

- [16] A. H. Walenta et al., *Nucl. Instrum. Methods* **92**, 373 (1971).
- [17] A. Breskin et al., *Nucl. Instrum. Methods* **119**, 9 (1974).
- [18] G. Marel et al., *Nucl. Instrum. Methods* **141**, 43 (1977); M. Holder et al., *Nucl. Instrum. Methods* **148**, 235 (1978).
- [19] D. R. Nygren, LBL Int. Report, Feb. 1974; J. N. Marx, D. R. Nygren, *Phys. Today*, Oct. 1978, p. 46.
- [20] WA 21-Collaboration using BEBC at CERN, Exp. WA 21 (1979).
- [21] L. Montanet, paper given at XXth Int. Conf. on High En. Physics, Madison, Wisconsin, July 1980.
- [22] L. S. Schröder, *Nucl. Instrum. Methods* **162**, 395 (1979).
- [23] P. Rice-Evans, *Spark, Streamer, Proportional and Drift Chambers*, London 1974.
- [24] V. Eckhardt, MPI München, private communication.
- [25] M. Dine et al., *Fermilab proposal No. 490*.
- [26] J. Sandweiss, paper given at XXth Int. Conf. on High En. Physics, Madison, Wisconsin, July 1980.
- [27] M. Conversi, A. Gozzini, *Nuovo Cimento* **2**, 189 (1955); M. Conversi, L. Federici, *Nucl. Instrum. Methods* **151**, 93 (1978).
- [28] F. E. Taylor et al., *IEEE Trans. Nucl. Sci.* **NS 25**, 312 (1978).
- [29] *Valuo Photomultiplier Book*, Hamburg, April 1970.
- [30] J. B. Birks, *Theory and practice of scintillation counting*, London 1964.
- [31] I. B. Berlman, *Fluorescence Spectra of Aromatic Molecules*, N. Y. and London 1971.
- [32] F. Klawonn, *Untersuchungen zur Optimierung der Szintillationszähler für den Einsatz in einem Hadronkalorimeter*, Universität Dortmund, Januar 1980.
- [33] R. C. Garwin, *Rev. Sci. Instrum.* **31**, 1010 (1960).
- [34] B. Barish et al., Very large area scintillation counters for hadron calorimetry, *IEEE Trans. Nucl. Sci.* **NS. 25**, 532 (1978).
- [35] H. P. Klasen, Diplomarbeit Universität Dortmund 1978.
- [36] P. A. Cerenkov, I. M. Frank, I. E. Tamm, *Nobel Lectures in Physics*, New York, Elsevier 1964.
- [37] M. Cantin et al., *Nucl. Instrum. Methods* **118**, 177 (1974).
- [38] J. Litt, R. Meunier, *Ann. Rev. Nucl. Sci.* **23**, 1 (1973).
- [39] V. L. Ginzburg, I. M. Frank, *JETP* **16**, 15 (1946).
- [40] X. Artru et al., *Phys. Rev.* **D12**, 1289 (1975); C. W. Fabjan, W. Struczinski, *Phys. Lett.* **57B**, 484 (1975).
- [41] G. M. Garibian, Proc. 5th Int. Conf., in *Instrumentation for High En. Phys.*, Frascati 1973, p. 329.
- [42] J. Cobb et al., *Nucl. Instrum. Methods* **140**, 413 (1977).
- [43] M. Deutschmann et al., *Particle identification using the angular distribution of transition radiation*, Preprint CERN EP/80-155, Aug. 1980.
- [44] Particle Data Group, *Phys. Lett.* **75B**, 1 (1978).
- [45] G. Bathow et al., *Nucl. Phys.* **B20**, 592 (1970).
- [46] M. Holder et al., *Nucl. Instrum. Methods* **151**, 69 (1978).
- [47] C. W. Fabjan et al., *Nucl. Instrum. Methods* **141**, 61 (1977).
- [48] P. Dishaw, *Limits on neutrino-like particles*, thesis Stanford University, 1979.
- [49] CERN-Dortmund-Heidelberg-Saclay-Collaboration (to be published); J. Rothberg, J. Wotschak, private communication.
- [50] G. Grayer, J. Homer (Rutherford Laboratory), private communication.
- [51] F. Eisele, K. Kleinknecht, D. Pollmann, B. Renk, Dortmund University.
- [52] NA 5 Bari-Cracow-Liverpool-München(MPI)-Nijmegen-Collaboration, CERN Proposal SPSC/75-1/P37.
- [53] V. Eckhardt et al., *Nucl. Instrum. Methods* **143**, 235 (1977).
- [54] UA 1 Aachen-AnneCy-Birmingham-CERN-London-Paris-Riverside-Rutherford-Saclay-Vienna-Collaboration, CERN Proposal SPSC/78-6, SPSC/P92.
- [55] E. Lorenz, private communication.